Interleukin-6 enhances localized immune cell infiltration and deep vein thrombosis resolution at the distal edge

Achyar, Arinal Chairul ; Hara, Tetsuya ; Adinata, Aditya ; Suzuki, Yoko ; Nishimori, Makoto ; Hirata, Ken-ichi ; Otake, Hiromasa ; Emoto,…

(Citation)
American Journal of Physiology-Heart and Circulatory Physiology,329(2):H603-H621

(Issue Date)
2025-08-01

(Resource Type)
journal article

(Version)
Version of Record

AMERICAN JOURNAL OF PHYSIOLOGY
HEART AND CIRCULATORY PHYSIOLOGY

Am J Physiol Heart Circ Physiol 329: H603–H621, 2025.
First published July 23, 2025; doi:10.1152/ajpheart.00163.2025

RESEARCH ARTICLE

Inflammation and Cardiovascular Disease

Interleukin-6 enhances localized immune cell infiltration and deep vein thrombosis resolution at the distal edge

Arinal Chairul Achyar,[1,2] Tetsuya Hara,[1,2] Aditya Adinata,[1,2] Yoko Suzuki,[2] Makoto Nishimori,[3] Ken-ichi Hirata,[1] Hiromasa Otake,[1] and Noriaki Emoto[1,2]

[1]*Division of Cardiovascular Medicine, Department of Internal Medicine, Kobe University Graduate School of Medicine, Kobe, Japan;* [2]*Laboratory of Clinical Pharmaceutical Science, Kobe Pharmaceutical University, Kobe, Japan; and* [3]*Division of Molecular Epidemiology, Kobe University Graduate School of Medicine, Kobe, Japan*

Abstract

Inflammation directed by immune cells is pivotal in the development of deep vein thrombosis (DVT). Disruption in the infiltration of these cells can lead to dysregulation of thrombus organization and increase the risk of deadly embolization. Although the general importance of the cytokine interleukin-6 (IL-6) in immune responses is well documented, its role in acute DVT remains largely unknown. Here, we elaborate on how IL-6 governs acute inflammation and the subsequent organization and early resolution of DVT in vivo. We induced DVT in mice via total inferior vena cava ligation and infused them with either recombinant IL-6 or phosphate-buffered saline (PBS) as a control. Exogenous IL-6 reduced DVT burden by 2 and 4 days with accelerated distal edge organization, characterized by well-demarcated fibrosis-like white lesions containing abundant fibrin-collagen, neutrophils, platelets, $Arg1^+$ monocytes, von Willebrand factor, laminin, myofibroblasts, and neovascular channels at the expense of erythrocytes. IL-6 upregulated intrathrombi chemokines, proinflammatory cytokines, and platelet-leukocyte surface markers in the distal region. This IL-6-heightened localized inflammatory response led to extracellular matrix remodeling, which is essential for DVT organization and early resolution. As observed by two-photon microscopy in stasis- and irradiation-induced saphenous vein thrombosis, IL-6 stimulated leukocytes to rapidly infiltrate the thrombus in parallel with venous flow through the distal edge. IL-6-augmented thrombus organization, visualized by rhodamine 6 G-labeled platelet-leukocyte accumulation, prompted early resolution, as determined by the reduced thrombus area. Ultimately, IL-6 enhances DVT organization by amplifying localized leukocyte migration and orchestrating acute inflammation involving platelets, thereby expediting the early resolution of DVT.

NEW & NOTEWORTHY IL-6 might play a beneficial role in acute DVT by coordinating the actions of innate leukocytes and platelets. This coordination enhances acute inflammation-dependent thrombus organization at specific distal locations, facilitating early resolution and reducing the burden of acute DVT. Although the role of inflammation in the pathogenesis of DVT remains controversial, our results indicate that IL-6 exerts an antithrombotic effect in acute DVT.

deep vein thrombosis; inflammation; interleukin-6; in vivo imaging; leukocyte

INTRODUCTION

Venous thromboembolism (VTE), comprising deep vein thrombosis (DVT) and pulmonary embolism (PE), occurs in ~1–2 per 1,000 patient-years among Western people and belongs to the top three leading causes of death globally (1, 2). Approximately 27%–56% of DVT cases progress to PE, which has a higher risk of mortality than the other 20%–50% of cases that end in chronic morbid post-thrombotic syndrome (2, 3). Although preventing PE is one of the primary goals of DVT management, addressing its contributing factors is noteworthy (4, 5). The risk of PE is augmented by a thrombus with low stability (6), even in the early DVT treatment by dabigatran, a thrombosis inhibitor that also inhibits fibrin cross linking, as demonstrated in a murine study (7). Accumulating evidence indicates that thrombus stability can be inferred from thrombus organization (8–10).

Emerging literature highlights the importance of immune cells and inflammatory responses involving chemokines, cytokines, and proteases in DVT organization, which consequently mandates resolution (11, 12). Along with platelets, the activation of innate immune cells plays a central role in eliciting inflammation (13). Platelets, through P-selectin, in addition to venous endothelial cells, accommodate leukocyte infiltration into the thrombus (mainly neutrophils and monocytes) during the acute phase (14, 15). Neutrophils

Correspondence: T. Hara (thara@kobepharma-u.ac.jp).
Submitted 7 March 2025 / Revised 31 March 2025 / Accepted 15 July 2025

release neutrophil extracellular traps (NETs) and, as with monocytes, inflammatory cytokines (15). Simultaneously, platelets secrete von Willebrand factor (vWF), which stabilizes the thrombus (9). Moreover, leukocytes promote fibrinolysis and degradation of cellular debris, leading to thrombus resolution (16, 17). Leukocyte recruitment is generally regulated by chemokines and/or cytokines, including monocyte chemotactic protein-1 (MCP-1) and interleukin-8 (IL-8). Experimental supplementation with these agents increases early intrathrombi leukocyte accumulation, resulting in enhanced organization and resolution, partly through angiogenesis (18, 19). Meanwhile, impaired leukocyte infiltration delays thrombus organization and resolution; hence, an immense DVT burden is unavoidable, as shown in neutropenic rats (20), *CXCR2*$^{-/-}$ mice (21), *CCR2*$^{-/-}$ mice (22), and *TLR4*$^{-/-}$ mice (23).

Beyond the involvement of innate immune cells in DVT, a growing body of literature indicates the contribution of adaptive immune cells. Mice lacking B cells exhibit increased thrombogenesis indirectly through neutrophilia and hyperfibrinogenemia (24). In addition, effector memory T cells that infiltrate the thrombosed vein wall secrete interferon-γ (IFN-γ) independently of antigen presentation, further inducing neutrophil and monocyte infiltration and hindering thrombus resolution (25). However, different subsets of T cells, CD4$^+$ and CD8$^+$ T cells (26), and specialized regulatory T cells (27) demonstrate an antithrombotic effect.

Widely known as a pleiotropic cytokine, interleukin-6 (IL-6) is generated locally at the injured tissue, mostly from myeloid cells (28), to facilitate an acute immune response by innate immune cells (29). During acute inflammation, IL-6 manages neutrophil trafficking, including recruitment and apoptosis, through STAT3 signaling (30). The leukocyte chemotactic response conferred by IL-6 has been shown to correlate with in situ chemokine secretion (31). Subsequently, IL-6 is responsible for the transition to a chronic immune response by adaptive immune cells. Although this mechanism often induces deleterious effects in various chronic inflammatory diseases, such as rheumatoid arthritis, systemic lupus erythematosus, and sarcoidosis (29, 32, 33), little is known about the role of IL-6 in DVT development.

Conflicting evidence exists regarding the contribution of IL-6 to DVT. IL-6 expression is elevated in the peripheral blood mononuclear cells of patients with DVT. Lowering IL-6 levels using an anti-IL-6 antibody or agomiR-338-5p impairs murine DVT formation (34). However, IL-6 blockade through genetic modification or pharmacological agents decelerates subacute thrombus resolution by reducing macrophage-derived proteolytic enzymes (35) and matrix metalloproteinase-9 (MMP-9) activity-induced recanalization (36). In chronic venous thrombosis, global depletion of IL-6 attenuates venous wall fibrosis. However, this effect is not observed following anti-IL-6 antibody administration. This indicates that IL-6 is not crucially involved in post-thrombotic syndrome (37). The investigation into the role of IL-6 during the initial days of DVT, covering the orchestration of immune cells toward thrombus organization and early resolution, is inadequate, underlining a knowledge gap that necessitates further exploration.

In recent years, advancements in thrombosis assessment by intravital imaging, including optical coherence tomography, positron emission tomography/computed tomography, confocal microscopy, epifluorescence microscopy, and two-photon microscopy, may have broken the barriers of DVT dynamics study in the acute time frame (38–41). In vivo imaging of a novel femoral/saphenous vein thrombosis model allows for temporal real-time observation of human-like DVT mechanisms involving inflammation (41). We thereby evaluated DVT organization and resolution with IL-6 treatment and harnessed molecular approaches along with intravital microscopy to elucidate IL-6-driven acute inflammation in DVT.

MATERIALS AND METHODS

Mice

Male C57BL/6J mice aged 8–12 wk and weighing 20–25 g (CLEA Japan, Inc.) were exclusively used in this study. Consistent with the fact that the incidence of first-episode VTE is higher in men than in women (42, 43), male mice also have a higher susceptibility to thrombosis, partly due to pulsatile growth hormone patterns that downregulate coagulation inhibitor genes in the liver (44). Considering the balance between scientific advancements and ethical animal treatment, where the interruption of the right branch of the inferior vena cava (IVC) as part of the model procedure does not compromise the male reproductive organs, in contrast to that in female mice, in which the right uterine vein drains to the IVC (45, 46), we decided to focus on male mice in this study. Mice allocated to the IVC ligation procedure were continuously infused with a subcutaneous mini-osmotic pump (ALZET model 1003 D or 2001; DURECT Corporation, Cupertino, CA) containing mouse recombinant IL-6 (rIL-6 BioLegend No. 575706/100 μg, San Diego, CA) at a dose of 1.2 μg/day or phosphate-buffered saline (PBS) as a control at an infusion rate of 1.0 μL/h starting a day before surgery until the day of DVT harvest. Mice designated for the femoral-saphenous vein thrombosis model were intraperitoneally injected with 0.3 μg rIL-6 in 200 μL PBS/mouse or 200 μL PBS/mouse as a control a day before thrombus induction. Mice were fed a standard chow diet, CFR-1 (Charles River Laboratories International, Inc., Wilmington, MA), and water ad libitum under a 12-h light-dark cycle. All experimental procedures carried out on mice were under the Kobe Pharmaceutical University Animal Experimentation Regulation and the Guide for the Care and Use of Laboratory Animals published by the US National Institute of Health (Publication No. 85-23, revised 1996) and have been approved by the Institutional Animal Care and Use Committee (2022-051, 2023-054, 2024-005).

IVC Ligation-Induced DVT

The mouse stasis-induced DVT model has been previously reported (47, 48). Mice were deeply anesthetized with continuous isoflurane (FUJIFILM Wako Pure Chemical, Osaka, Japan) inhalation (2 L/min). Following the midline laparotomy procedure, the intestines were laterally displaced to expose the retroperitoneal space, in which the aorta was freely separated from the IVC. Total ligation was performed on the infrarenal IVC with a 6-0 nylon suture and on its right branch with a 7-0 nylon suture to induce complete cessation of venous blood flow. Consequently, thrombogenesis occurs steadily and relatively faster with a pronounced vein wall

reaction, leading to a more even thrombus size and homogeneous intrathrombi composition (45, 49, 50) compared with the IVC stenosis model, where partial venous occlusion occurs (51, 52). The mice were euthanized on *days 2* or *4* after IVC ligation. We harvested the infrarenal IVC to collect vein wall-free and vein wall-lined thrombi for specific studies. Macroscopic images and length and weight measurements were obtained after thrombus harvest. Thrombi were then stored in 4% paraformaldehyde (PFA) overnight, followed by a 4-h immersion in 30% sucrose solution before embedding in the Tissue-Tek optimal cutting temperature (OCT) compound (Sakura Finetek, 4583) for histopathological analyses, or snap frozen and stored at −80°C for quantitative polymerase chain reaction (PCR) and protein assays.

Histopathology Analyses

Basic histology.

The OCT-embedded thrombus tissues were sectioned using a Leica CM1860 cryostat (Leica Biosystems, Nussloch, Germany) at 6–8 μm thick. Hematoxylin-eosin (HE) staining was performed to evaluate the gross histological features of the longitudinal thrombus sections. Carstairs staining was performed to differentiate the composition of the longitudinal thrombus sections: red blood cells (yellow), fibrin (red), platelets (gray), and collagen (blue). Picrosirius red staining (0.5 g of Sigma-Aldrich 365548-5 G Direct Red 80 Dye in 500 mL of a saturated aqueous solution of picric acid) was performed to evaluate the collagen thickness of the vein wall at the axial section of the thrombosed IVC.

Immunohistochemical staining.

After removing OCT through quick distilled water immersion, heat-induced epitope retrieval was performed by immersing the PFA-fixed thrombus sections in antigen-unmasking solution (citric acid-based) H-3300 (Vector Laboratories, ZE0905), heated at 90°C–95°C for 10 min. Endogenous peroxidase activity was blocked by immersing the thrombus sections in 3% H_2O_2 in methanol. To enhance reaction specificity, the sections were incubated with 10% normal serum (in 0.1% PBS-Triton X) of the origin species of the secondary antibodies for an hour at room temperature. The 4°C overnight incubation with rat anti-mouse NIMP-R14 (Santa Cruz sc-59338, 1:100 dilution), rabbit anti-mouse Arg1 (Proteintech 16001-1-AP, 1:200 dilution), rabbit anti-mouse CCR2 (Abcam ab273050, 1:250 dilution), rabbit anti-mouse CD61 (Novus Biologicals NBP2-67416, 1:200 dilution), rabbit anti-mouse vWF (Abcam ab9378, 1:50 dilution), rabbit anti-mouse SM22α (Abcam ab14106, 1:200 dilution), and rabbit anti-mouse laminin (Abcam ab11575, 1:200 dilution), continued with an hour incubation of biotinylated secondary antibodies at ambient temperature, was conducted to detect neutrophils, proreparative monocytes, inflammatory monocytes, platelets, vWF, myofibroblasts, and laminin, respectively. Antigen-antibody binding was observed using diaminobenzidine (Vector Impact DAB peroxidase substrate kit; Vector Laboratories, SK-4105) and counterstained with Gill's hematoxylin (Muto Chemical, 30051).

Immunofluorescence.

OCT removal and heat-induced epitope retrieval for PFA-fixed thrombus sections were performed similarly to immunohistochemical staining. The sections were then incubated with 5% donkey serum (in 0.1% PBS-Triton X) for an hour at room temperature. The 4°C overnight incubation with the combinations of rat anti-mouse NIMP-R14 (Santa Cruz sc-59338, 1:100 dilution) and rabbit anti-mouse CD19 (Cell Signaling Technology 3574S, 1:100 dilution) or rabbit anti-mouse CD3ε (Abcam ab16669, 1:100 dilution); rat anti-mouse CD31 (BD Pharmingen 550274, 1:100 dilution) and rabbit anti-mouse SM22α (Abcam ab14106, 1:200 dilution), continued with an hour incubation of fluorochrome-labeled secondary antibodies in the dark at room temperature, was performed to assess the population of B cells or T cells in the surroundings of neutrophils and venous endothelial cells that undergo myofibroblast transition, respectively. Vectashield mounting medium with DAPI (Vector Laboratories, H-1200-10) was then applied.

All stained sections were visualized and captured using an All-in-One Fluorescence Microscope (BZ-X810; Keyence) and the associated software (BZ Analyzer software; Keyence). Fiji software (National Institute of Health, Bethesda, MD) was used to quantify the RBC, fibrin, collagen, $CD61^+$ platelet, vWF, $SM22\alpha^+$, and laminin areas as a percentage of the corresponding area of the thrombus. Vein wall thickness was measured on five fields radially around the IVC under ×22.2 magnification of the objective lens and averaged. The numbers of $NIMP\text{-}R14^+$ neutrophils, $CD19^+$ B cells, $CD3\varepsilon^+$ T cells, $Arg1^+$ monocytes, and $CCR2^+$ monocytes were taken from five fields under ×22.2 magnification of the objective lens, and laminin-positive channels were taken from five fields under ×44.4 magnification of the objective lens, counted, and totaled with adjustment to the total measured area. The fluorescence intensities of CD31 and SM22α were measured in five fields radially around the IVC under ×22.2 magnification of the objective lens, averaged, and normalized to the PBS group.

Quantitative Real-Time PCR

RNAs were extracted from the thrombus tissues (whole tissue or ⅓ distal part) using RNAiso Plus (Takara Bio) and purified using the NucleoSpin RNA Clean-Up kit (Macherey-Nagel). cDNA was synthesized from 1 μg of total RNA using the PrimeScript RT Reagent Kit with a gDNA eraser (Takara Bio). Quantitative real-time PCR was performed using a LightCycler96 (Roche Applied Science) with TB Green Premix Ex Taq II [Tli RNaseH Plus; Takara Bio RR820B(Ax2)]. The mRNA expression levels of the target genes were normalized to 18s levels, analyzed using the $2^{-\Delta\Delta CT}$ method (53), and expressed in arbitrary units. All primers used for quantitative real-time PCR are listed in Supplemental Table S1.

Enzyme-Linked Immunosorbent Assay

Interleukin-6.

On the day of DVT harvest, the vein wall-free thrombi were homogenized in lysis buffer (25 mM Tris-HCl, pH 7.5, 100 mM NaCl, and 1% Nonidet P-40) containing a protease inhibitor (Sigma-Aldrich, P8340). The homogenates were centrifuged at 15,000 rpm for 15 min. The total protein concentration was measured using the DC protein assay kit from Bio-Rad No. 5000116. IL-6 levels in the thrombus lysates and

citrated plasma were measured using the ELISA MAX Deluxe Set Mouse IL-6 (BioLegend No. 431304) according to the manufacturer's protocol, with a sensitivity of 2 pg/mL. The intrathrombi IL-6 levels were normalized to the total protein concentration and expressed as pg/μg of total protein, and plasma IL-6 levels were expressed as pg/mL.

Von Willebrand factor.

Heparinized plasma collected on the days of DVT harvest was subjected to vWF level measurement using the Mouse von Willebrand Factor SimpleStep ELISA kit (Abcam ab314372) according to the manufacturer's protocol. The sensitivity was 0.045 ng/mL. Plasma vWF levels were expressed as μg/mL.

Intrathrombi MMP Activity

Sodium dodecyl sulfate-polyacrylamide gel electrophoresis gelatin zymography.

Gelatinase (MMP-2 and MMP-9) activity was evaluated using a protocol adapted from a previous study (54). In brief, 1.25 μg of protein lysates from the whole part of *day 4* vein wall-free thrombi were subjected to gelatin zymography using 10% sodium dodecyl sulfate-polyacrylamide gels containing 1 mg/mL of gelatin. SDS-PAGE was performed at a constant voltage of 150 V for 50–60 min in a running buffer composed of 25 mM Tris, 192 mM glycine, 0.1% (wt/vol) SDS, and pH 8.3. After electrophoresis, the gels were extracted and immersed twice in a buffer containing 2.5% (vol/vol) Triton X-100, 50 mM Tris-HCl, pH 7.5, 5 mM $CaCl_2$, and 1 μM $ZnCl_2$ for 30 min each to renature the enzymes. Subsequently, the gels were incubated overnight at 37°C in a solution of 1% (vol/vol) Triton X-100, 50 mM Tris-HCl, pH 7.5, 5 mM $CaCl_2$, and 1 μM $ZnCl_2$ to facilitate gelatinolytic activity. Subsequently, the gels were treated with 10% (vol/vol) 2,2,2-trichloroethanol (TCE) in a 1:1 methanol-water mixture for 10 min. Stain-free TCE-visualized total proteins were imaged using a ChemiDoc XRS Plus (Bio-Rad). The gels were then stained with Coomassie [0.5% (wt/vol) Coomassie Brilliant Blue R-250, 40% (vol/vol) methanol, and 10% (vol/vol) acetic acid] for 30 min, followed by destaining [40% (vol/vol) methanol and 10% (vol/vol) acetic acid] until distinct bands appeared, after which the gels were imaged using ChemiDoc XRS Plus (Bio-Rad). The optical densities of MMP-2, MMP-9, and total gelatinolytic activity were normalized to total protein signals in each sample, as determined by densitometry of stain-free illumination.

Ex vivo imaging of intrathrombi MMP activity.

MMP activity was assessed as previously described (39, 55). In brief, a day before the *day 4*-DVT harvest, 2 nmol/150 μL 1× PBS of MMPSense 680 (NEV10126, PerkinElmer) was administered to each mouse via retroorbital injection. The vein wall-free thrombi were visualized under an IVIS Spectrum imaging system (Lumina LT, PerkinElmer) at an excitation wavelength of 670 nm and an emission wavelength of 620 nm to detect the intrathrombi MMPs (including MMP-2, -3, -9, and -13)-driven activation of MMPSense 680 and subsequently processed with the associated software (Living Image 4.4, PerkinElmer). The level of intrathrombi MMP activity was determined by the target-to-background ratio, formulated as the mean signal intensity of the thrombus divided by the mean signal intensity of the heart of the corresponding mouse and expressed in arbitrary units.

Stasis- and Irradiation-Induced Saphenous Vein Thrombosis

A new mouse venous thromboembolism model, which combines stasis and irradiation of the femoral/saphenous veins and uses serial in vivo imaging, has been previously described (41). The mice were anesthetized with continuous isoflurane inhalation (2 L/min) and placed on a customized board in a supine position. The femoral skin was incised, and the surrounding connective tissue was removed to expose the femoral/saphenous vein and artery. The femoral vein located proximally to the venous bifurcation was cautiously liberated from the femoral artery and completely ligated with 7-0 nylon sutures to induce stasis blood flow. All mice that suffered from profound bleeding were excluded from further experiments.

The mice were then positioned on the stage of epifluorescence microscopy, with the saphenous vein as the main focus of visualization using fluorescein isothiocyanate (FITC)-dextran. The saphenous vein was perpetually irradiated with FITC-filtered light through a ×10 objective lens every 5 s for 60 s to initiate and image DVT formation. A minimal amount of PBS was applied to the exposed tissues throughout in vivo imaging.

Intravital Epifluorescence Microscopy

A Nikon multichannel epifluorescence microscope (Nikon Eclipse Ni; Nikon, Tokyo, Japan) with ×4 (Plan Fluor, NA 0.13) and ×10 (Plan Fluor, NA 0.3) objective lenses and the associated software (NIS Elements software; Nikon) was used to perform intravital imaging of the blood circulation in living mice. This system has a mercury lamp for excitation at 350/50, 475/35, 542/20, and 630/38 nm (Nikon Intensilight C-HGFIE; Nikon), which is coupled to filters for DAPI, FITC, TRITC, and Cy5, respectively. A handheld laser check power meter (Coherent, Japan) was used to assess the total power density of each filtered light using a ×10 objective lens, yielding DAPI (15 mW/mm^2), FITC (16 mW/mm^2), TRITC (16 mW/mm^2), and Cy5 (4 mW/mm^2).

Blood flow in the mice was visualized by injecting FITC-dextran (FD2000S, Sigma-Aldrich, St. Louis, MO) at a dose of 25 mg/kg retroorbitally, resulting in a view of dye-free blood cells. Rhodamine 6 G (2.5 mg/kg; Santa Cruz Biotech Inc., Dallas, TX) was administered with FITC-dextran 10–15 min before live imaging to label the circulating leukocytes and platelets. BUV563 rat anti-mouse Ly6G/Ly6C (0.1 mg/kg; 741226, BD Biosciences) and DyLight 649-conjugated rat anti-mouse CD42b (GPIbα, 0.1 mg/kg; X649, Emfret Analytics, Eibelstadt, Germany) were administered in the same manner to specifically illuminate $Ly6G^+Ly6C^+$ leukocytes and platelets, respectively.

Venous Blood Flow Velocity Assessment

Erythrocytes were labeled with FITC Isomer I (F7250, Sigma-Aldrich, MO) using a protocol adapted from a previous study (41). Whole blood was extracted from a donor mouse through heart puncture using a heparinized syringe and subjected to centrifugation at 200 *g*/min for 10 min at

20°C. The supernatant was discarded, and the cells underwent two washing cycles of 5 min centrifugation at 200 *g*/min, 20°C in PBS containing 0.5 mM Na_2-EDTA (pH 8.0). Subsequently, the erythrocytes were incubated with FITC Isomer I (1 mg/mL PBS-EDTA) for 2 h at room temperature. Postincubation, the supernatant dye was eliminated by centrifugation at 200 *g*/min for 5 min, followed by three washes with PBS-EDTA. The labeled erythrocytes were adjusted to a final hematocrit of 20%–30% using PBS-EDTA and could be stored at 4°C for 24 h. FITC Isomer I-labeled erythrocytes (100 μL) were injected retroorbitally following ligation of the femoral vein of a recipient mouse, and blood flow in the saphenous vein was recorded under an epifluorescence microscope on a ×10 objective lens at four times lower laser intensity than used for thrombogenesis, at a rate of ∼8.7 frames/s. At least five representative erythrocytes were tracked in 30 successive frames in each mouse using the Fiji software manual tracking plug-ins (National Institute of Health, Bethesda, MD). Blood flow velocity (μm/s) was calculated as the distance covered by FITC Isomer I-labeled erythrocytes divided by time, and the mean value for each mouse in both groups was pooled for statistical analysis.

Saphenous Vein Thrombosis Resolution Analysis

DVT was identified as a filling deficiency on FITC-dextran-generated venograms. The DVT region was traced and divided into ⅓ distal area, ⅓ proximal area, and the whole area by denoting the lateral vessel as an anatomical landmark, and measured using Fiji software. The same lesion was scanned after 2 and 24 h, as specified in each experiment, to evaluate DVT resolution in terms of DVT area reduction over time.

Intravital Two-Photon Microscopy

The two-photon microscope imaging system was built using an upright two-photon microscope (Zeiss LSM 7 MP) powered by a laser (Coherent Chameleon Ti:Sapphire; Glasgow, UK) tuned to 860 nm and a ×40/1.0 water-immersion objective lens (W Plan-Apochromat DIC M27). Fluorescence signals were detected using two external non-descanned detectors with the following emission filters: 492/SP nm for SHG (blue channel), 525/50 nm for FITC-dextran, and 575/25 nm for rhodamine 6 G (red channel). The laser intensity varied from 12 to 18 mW. The system processed 3-color pictures (512 × 512 pixels) at a rate of 7 frames/s. Image stacks were acquired at 0–100 μm depth below the saphenous vein surface using a 3-μm vertical step. Time-lapse imagery was captured every minute for 20–30 min. Raw imaging data were processed using ZEN 2011 software.

Intravital Leukocyte Infiltration Assay

Fiji software (National Institute of Health, Bethesda, MD) was used to generate three-dimensional time-lapse videos using two-photon image stacks. Semiautomated tracking of the motility of rhodamine 6 G-positive leukocytes that infiltrated DVT in three dimensions (*x*, *y*, and *t*) was performed using the TrackMate plugin (56, 57). The distance traveled was determined by recording the positions at the initial and final points of the migration tracking. These positions were measured along the *x*-axis concerning the saphenous vein midline and the *y*-axis concerning venous flow. The migration speed was calculated by dividing the distance by the time.

Complete Blood Count and Coagulation Profile Assay

Blood was collected from the mice's hearts a day after rIL-6 or PBS administration using a 1 mL syringe with a 26 G needle mixed with EDTA to measure the baseline complete blood count. On the day of DVT harvest, bleeding time was assessed using the tail vein filter paper method, as previously explained (58). Blood collected from cardiac puncture was mixed with 3.8% sodium citrate at a ratio of 1:9 and centrifuged at 1,000 *g* for 10 min to obtain plasma samples for the coagulation profile assay. The measurement was delegated to Fujifilm and performed according to their procedures.

Statistical Analyses

All data are presented as means ± standard error (SE). The Shapiro–Wilk test was performed to determine the normality of the data distribution. To evaluate the mean difference between IL-6-treated and control groups, the unpaired *t* test with Welch's correction was used for parametric data; otherwise, the Mann–Whitney test was used. A two-way ANOVA with Tukey's multiple comparisons was conducted to determine the mean difference between the two groups at various time points. A mixed-effects model was used to evaluate changes in the thrombus area in the stasis- and irradiation-induced DVT model. Time points, groups, and their interactions were considered fixed variables, and mice were considered random variables. Statistical significance was defined as $P < 0.05$. All statistical analyses were performed using GraphPad Prism 8.0.1 (GraphPad Software, Inc., California).

RESULTS

IL-6 Administration Decreases DVT Burden

To investigate the role of IL-6 in DVT burden, we administered rIL-6 using a mini-osmotic pump a day before inducing DVT through the harvest day on *days 2* or *4* (Fig. 1*A*). Baseline complete blood count analyses revealed no significant differences between the IL-6 and PBS groups (Supplemental Table S2). Surprisingly, IL-6-treated mice formed a substantially smaller IVC thrombus in terms of length, weight, and adjusted weight/length than PBS-treated mice (Fig. 1, *B*–*G*). IL-6-treated mice had significantly higher plasma and intrathrombi IL-6 levels than controls, confirming an effective continuous delivery of rIL-6 (Supplemental Fig. S1, *A* and *B*). Nevertheless, both groups of mice showed similar bleeding times and coagulation profiles, as shown by prothrombin time, activated partial thromboplastin time, and fibrinogen levels (Supplemental Table S3). These findings suggest that exogenous IL-6 abates DVT propagation, leading to a reduction in the DVT burden.

IL-6 Does Not Alter the Whole DVT Architecture

To understand why IL-6 decreased DVT size, we performed histological analyses of the resected DVT. The whole thrombi were harvested by separating the surrounding vein wall to observe the distribution of the tissue components (Supplemental Fig. S1*C*). Both groups of mice demonstrated

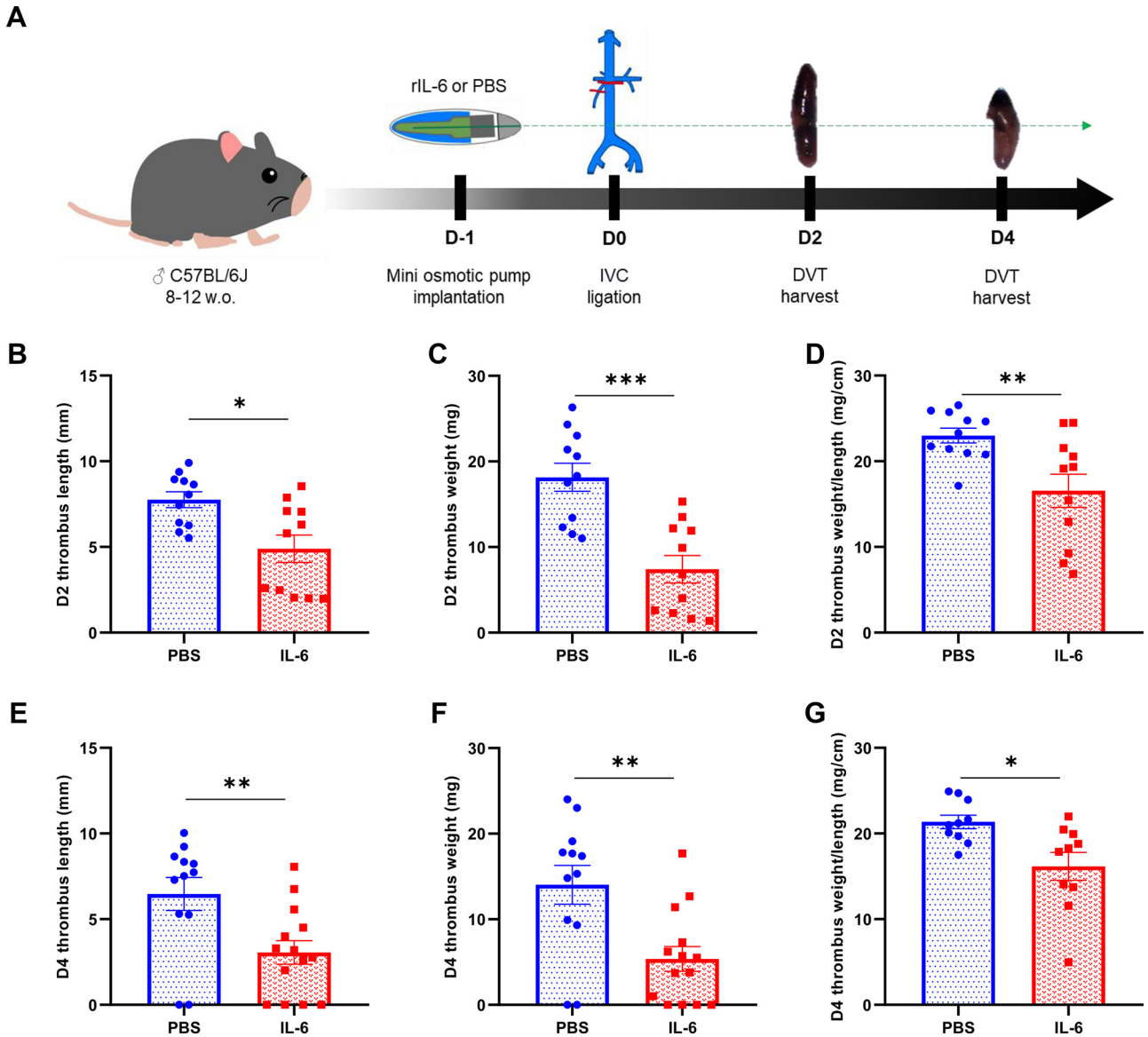

Figure 1. Exogenous IL-6 reduces the burden of deep vein thrombosis (DVT) in an inferior vena cava (IVC) stasis model. *A*: schematic diagram illustrating the experimental design. Total ligation was performed on the infrarenal inferior vena cava (IVC) and its right branch of C57BL/6J mice a day after the initiation of continuous infusion of recombinant interleukin-6 (rIL-6) or phosphate-buffered saline (PBS). Vein wall-free thrombi were pathologically analyzed on *days 2* or *4* after IVC ligation. Images were sketched using a licensed version of Goodnotes 6.6.10. *B*: length of thrombi measured on *day 2* ($n = 11$ mice/group). *C*: weight of thrombi harvested on *day 2* ($n = 11$ mice/group). *D*: weight of thrombi harvested on *day 2* was adjusted to length ($n = 11$ mice/group). *E*: length of thrombi measured on *day 4* ($n = 12$–14 mice/group). *F*: weight of thrombi harvested on *day 4* ($n = 12$–14 mice/group). *G*: weight of thrombi harvested on *day 4* was adjusted to length ($n = 10$ mice/group). Data are presented as means ± standard error (SE). Statistical analysis was performed using the unpaired *t* test with Welch's correction (*C*, *D*, *F*, and *G*) and the Mann–Whitney test (*B* and *E*); $^{*}P < 0.05$, $^{**}P < 0.01$, $^{***}P < 0.001$. IL-6, interleukin-6.

a similar amount of white lesion area on *days 2* and *4* (Supplemental Fig. S1*D*). HE and Carstairs staining of the longitudinal sections of thrombi showed that the erythrocyte content diminished, whereas the increase in fibrin-collagen deposition occurred from *day 2* to *day 4* after IVC ligation in both groups (Supplemental Fig. S1, *E*–*H*). Immunostaining revealed that the numbers of intrathrombi NIMP-R14^{+} neutrophils, CD19^{+} B cells, CD3ε^{+} T cells, Arg1^{+} monocytes, CCR2^{+} monocytes, CD61^{+} platelets, and vWF deposition were equivalent in the whole thrombus in both groups (Supplemental Fig. S2, *A*–*L*). Circulating vWF levels also showed unremarkable changes upon IL-6 treatment (Supplemental Fig. S2*M*). Accordingly, these histological staining results clarified that the macroscopic white lesion represented a fibrosis-like area densely populated with neutrophils and platelets (Supplemental Fig. S3).

We extended our analyses using real-time PCR for a better quantitative approach. IL-6-treated mice shared a similar expression level of intrathrombi mRNA of IL1β, CXCL2, MCP1, and TNFα as the proinflammatory cytokines and chemokines; Mac-1, GPIbα, PSGL-1, and SELP as leukocyte and platelet activation markers; and F4/80 (Adgre1), RANTES (CCL5), and TGFβ1 as the genes involved in extracellular matrix regulation with PBS-treated mice (Supplemental Fig.

S4, *A*–*C*). These data indicate that IL-6-induced DVT size reduction might result from localized actions rather than gross architectural changes.

IL-6 Enhances DVT Organization at the Distal Edge

After reassessing the gross macroscopic pictures of DVT, we found that DVT from IL-6-treated mice exhibited appealingly well-organized white lesions at the distal edge of DVT (Fig. 2*A*). Therefore, we reanalyzed the pathobiological profile of the thrombi, considering the possibility of the segmented effect of IL-6 relative to the venous blood flow direction by scrutinizing the ⅓ distal part of the thrombus (Fig. 2*B*). Quantitative analyses confirmed that the white lesions on the distal part of DVT from IL-6-treated mice, which progressed from *day 2* to *day 4*, were substantially more extensive in contrast to those in PBS-treated mice (Fig. 2*C*). This macroscopic feature suggests that IL-6 locally promotes DVT organization in the distal part of the thrombus.

DVT organization is a time-course process of shifting the erythrocyte-rich thrombus to a more compact and stable tissue matrix-rich thrombus (9, 59). The IL-6-treated mice's thrombus showed vivid demarcation by the ⅓ distal part, which contained a significantly smaller erythrocyte area and larger fibrin-collagen area than the PBS-treated mice's thrombus, indicating accelerated organization (Fig. 2, *D*–*G*).

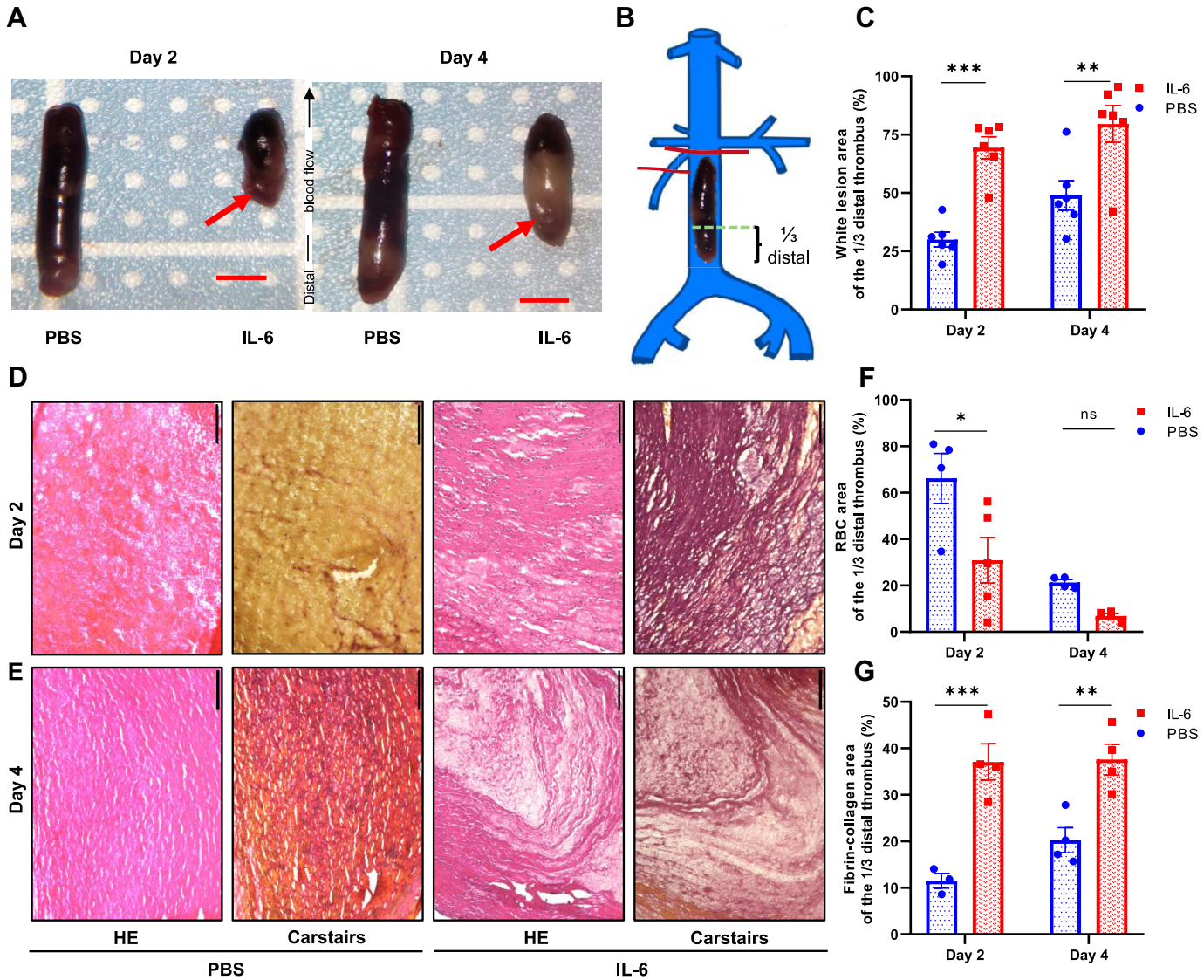

Figure 2. IL-6-treated mice exhibit an accelerated thrombus organization at the distal edge. *A*: representative macroscopic images demonstrating white lesions (red arrow) found in the distal edge of the thrombus in IL-6-treated mice (scale bar = 2 mm). *B*: schematic of the thrombus segment for analysis: ⅓ distal part. Images were sketched using a licensed version of Goodnotes 6.6.10. *C*: the extent of the white lesion was quantified on the ⅓ distal thrombus part and expressed as the percentage of the corresponding area. *D*–*G*: vein wall-free thrombi aged 2 and 4 days in PBS- and IL-6-treated mice were longitudinally frozen-sectioned and stained with hematoxylin-eosin and Carstairs. Representative histological images of the ⅓ distal thrombus part (*D* and *E*; ×22.2 magnification; scale bar = 100 μm) with the corresponding quantifications of red blood cells (RBCs; yellow) and fibrin-collagen (red-blue) area (*F* and *G*, respectively). Data are presented as means ± standard error (SE). Statistical analysis was performed using two-way ANOVA with Tukey's multiple-comparisons test (*C*, *F*, and *G*); $^{*}P < 0.05$, $^{**}P < 0.01$, $^{***}P < 0.001$; ns, nonsignificant; $n = 3$–7 mice/group. HE, hematoxylin-eosin; IL-6, interleukin-6; PBS, phosphate-buffered saline.

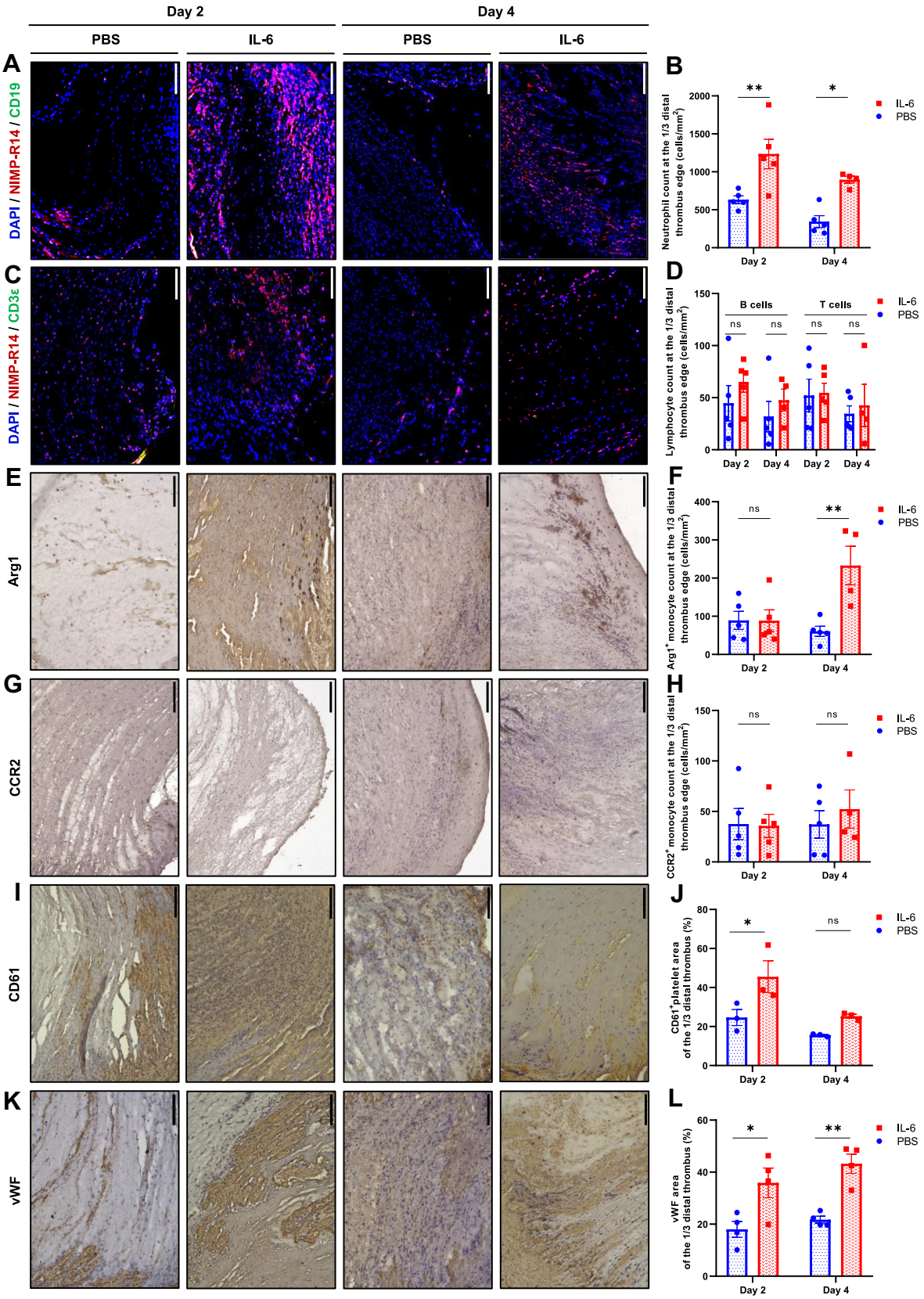

As these histological features were linear to the macroscopic findings, we postulate that the distal edge of the thrombus is the primary locus of IL-6-mediated enhanced organization.

IL-6 Enhances the Distal Accumulation of Acute Immune Cells in the Thrombus

Neutrophils and monocytes are the initial immune cells that present with platelets in the early days of DVT (15, 60, 61). Immunofluorescence staining revealed that IL-6-treated mice demonstrated a significantly greater accumulation of neutrophils in the distal part of the thrombus on *days 2* and *4* than in the PBS group without impacting the recruited numbers of B cells and T cells (Fig. 3, *A–D*). Notably, pro-reparative Arg1$^+$ monocytes, not inflammatory CCR2$^+$ monocytes, incrementally localized at the distal edge of the thrombus by *day 4* in response to IL-6 (Fig. 3, *E–H*). CD61$^+$ activated platelets aggregated in correspondence with the neutrophil-rich distal edge of the IL-6-treated mice's thrombus, mainly on *day 2* and slightly declined on *day 4* (Fig. 3, *I* and *J*). Moreover, vWF was expressed in a distribution pattern identical to that of neutrophils and platelets (Fig. 3, *K* and *L*). These results suggest that IL-6 accelerates the organization of the distal edge of the thrombus by alluring neutrophils and platelets with the associated vWF deposition and subsequently, pro-reparative monocytes.

IL-6 Upregulates Inflammation and Matrix Remodeling at the Distal Edge of the Thrombus

Quantitative real-time PCR was performed to ascertain the mechanism by which IL-6 governs thrombus organization at the distal edge. We observed that in response to exogenous IL-6, IL1β, and CXCL2, the proinflammatory cytokines and chemokines for neutrophils were notably upregulated at the mRNA level in the thrombus distal edge 2 days after IVC ligation relative to that in PBS-treated mice. By 4 days following DVT induction, which is reported as the transition day of polymorphonuclear leukocytes (PMNs) to the mononuclear leukocyte population (62), we found that the mRNA expression of the proinflammatory cytokines MCP1 and TNFα was significantly elevated in the IL-6-treated mice's thrombus distal edge compared with that in the PBS-treated mice (Fig. 4*A*). Moreover, the mRNA expression of the monocyte/macrophage surface marker F4/80 (Adgre1) was noticeably increased in the distal edge of the 4-day-aged thrombus in IL-6-treated mice (Fig. 4*C*). We observed similar vein wall thickness and endothelial-to-mesenchymal transition (EndMT) between the IL-6 and PBS-treated groups (Supplemental Fig. S4, *D–H*). These data demonstrate that IL-6 guides neutrophil-to-monocyte-driven inflammation at the distal edge of the thrombus.

In addition, we identified a marked increase in Mac-1 transcripts on *day 4*, GPIbα on *days 2* and *4*, PSGL-1 on *days 2* and *4*, and SELP on *day 4* within the distal part of the IL-6-treated mice's thrombus relative to that in PBS-treated mice (Fig. 4*B*), implying IL-6-induced activation of leukocytes and platelets. As their interactions were recently identified in the resolution process following the initiation of inflammation (63), we examined the intrathrombi expression of extracellular matrix regulator genes. By *day 2* of stasis-induced IVC thrombosis, TGFβ1 transcripts increased within the distal part of the IL-6-treated mice's thrombus. Furthermore, the mRNA expression of RANTES (CCL5) and TGFβ1 was elevated at *day 4* in the thrombus distal edge of IL-6-treated mice compared with that in the PBS-treated mice (Fig. 4*C*), indicating remodeling of the thrombus extracellular matrix, which is essential for the organization and early resolution of the thrombus (64). These findings demonstrate that IL-6 regulates inflammation through platelet-leukocyte interactions to organize thrombi.

To evaluate the effects of IL-6 on extracellular matrix remodeling within the thrombus, we performed immunohistochemical staining targeting myofibroblasts, which are key players in this process (65, 66), and laminin, an extracellular matrix component (67). The distal edge of the thrombus in IL-6-treated mice exhibited a greater SM22α-positive area as early as *day 2*, indicating myofibroblast activity (Fig. 5, *A* and *B*). This activity might be independent of the EndMT process (Supplemental Fig. S4, *F–H*). Laminin was considerably more extensive at the distal edge of the thrombus in IL-6-treated mice (Fig. 5, *C* and *D*). However, the SM22α-positive population and laminin area over the whole thrombus did not differ between the groups (Supplemental Fig. S5, *A–D*). These findings corroborate the pattern of fibrin-collagen deposition (Fig. 2, *D, E, G*; Supplemental Fig. S1, *E, F*, and *H*).

Tissue remodeling is widely associated with neovascularization (61, 68). By *day 4*, neovascular channels were substantially detected within the distal edge of the thrombus in IL-6-treated mice (Fig. 5, *E–G*), consistent with the presence of pro-reparative monocytes (Fig. 3, *E* and *F*). Nonetheless, we could not detect the upregulation of VEGFA and MMP transcripts on *day 4* (data not shown). Further analysis through gelatin zymography revealed a slight trend toward higher MMP-9 activity than MMP-2 activity in the whole thrombus, with comparable total gelatinolytic activity (Supplemental Fig. 5, *E–I*). This finding was confirmed by fluorescence visualization of MMP activity in both groups of mice (Supplemental Fig. 5, *J* and *K*).

In Vivo DVT Imaging Demonstrates Acute Immune Cell Recruitment and Subsequent Thrombus Resolution in Response to IL-6

The stasis- and irradiation-induced femoral/saphenous vein thrombosis model enables the sequential evaluation of acute DVT organization and early resolution by considering the prompt involvement of immune cells (41, 69). Hence, we used epifluorescence microscopy to elucidate how IL-6 orchestrates the acute recruitment of innate immune cells into the

Figure 3. Immune cells accumulate at the IL-6-induced, organized, distal edge of the thrombus. *A–L*: vein wall-free thrombi aged 2 and 4 days from PBS- and IL-6-treated mice were longitudinally frozen-sectioned and stained for NIMP-R14 (*A* and *B*; red), CD19 (*A* and *D*; green), CD3ε (*C* and *D*; green), Arg1 (*E* and *F*), CCR2 (*G* and *H*), CD61 (*I* and *J*), and von Willebrand factor (vWF) (*K* and *L*). Representative images of the ⅓ distal thrombus part (*A*, *C*, *E*, *G*, *I*, *K*; ×22.2 magnification; scale bar = 100 μm) with the corresponding quantifications of NIMP-R14$^+$ neutrophils, CD19$^+$ B cells, CD3ε$^+$ T cells, Arg1$^+$ monocytes, CCR2$^+$ monocytes, CD61$^+$ platelet area, and vWF area (*B*, *D*, *F*, *H*, *J*, and *L*, respectively). Blue (*A* and *C*), nuclear staining with 4′,6-diamidino-2-phenylindole (DAPI). Data are presented as means ± standard error (SE). Statistical analysis was performed using two-way ANOVA with Tukey's multiple-comparisons test (*B*, *D*, *F*, *H*, *J*, and *L*); $*P < 0.05$, $**P < 0.01$; ns, nonsignificant; $n = 3–5$ mice/group. IL-6, interleukin-6; PBS, phosphate-buffered saline.

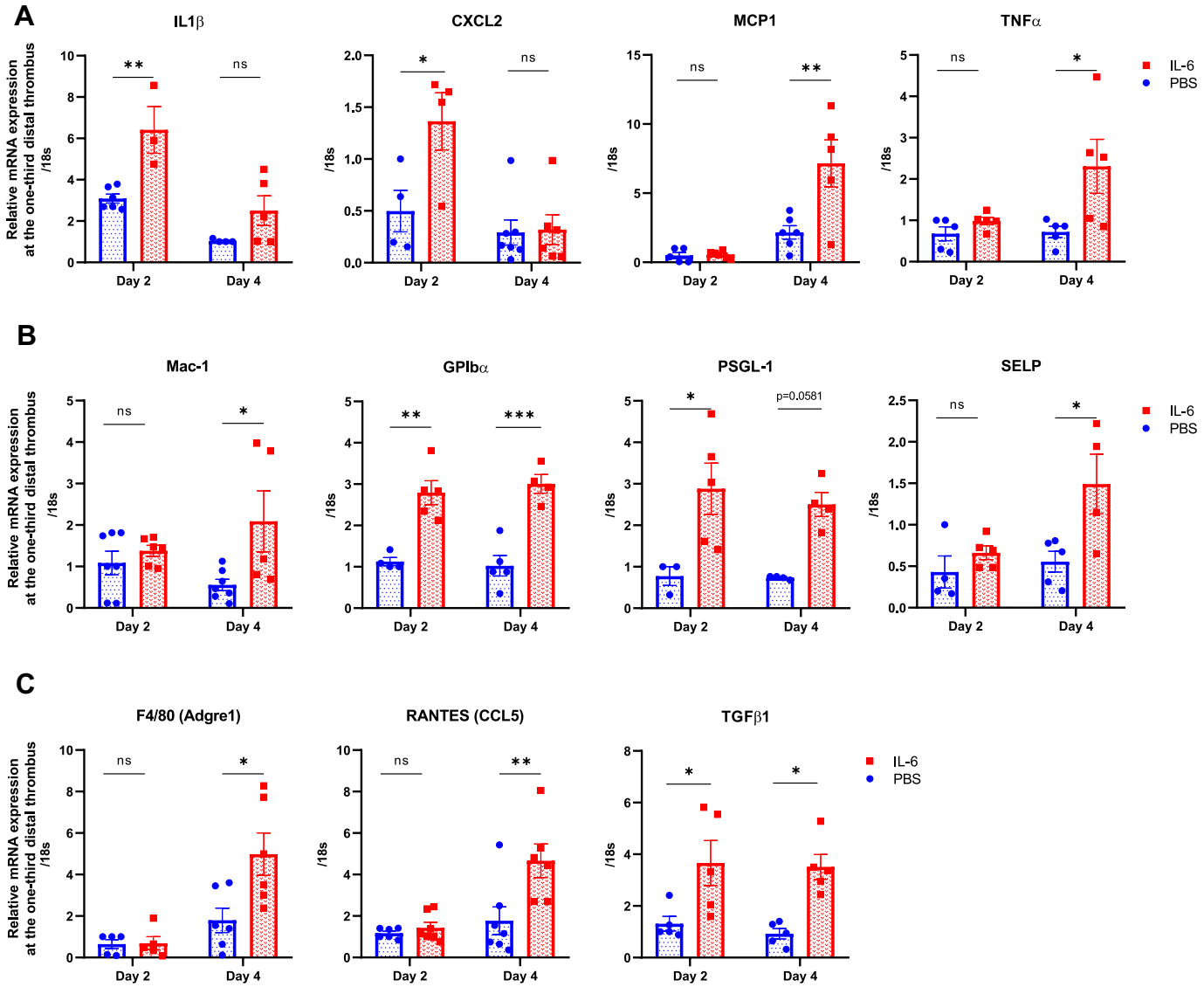

Figure 4. The IL-6-driven inflammatory response at the distal edge of the thrombus is linked to augmented DVT organization. *A*–*C*: the ⅓ distal part of vein-wall-free thrombi aged 2 and 4 days in PBS- and IL-6-treated mice were extracted and purified for RNA with subsequent cDNA processing for quantitative polymerase chain reaction (PCR) analyses of leukocyte chemoattractants (*A*), markers of interaction between leukocytes and platelets (*B*), and genes regulating tissue matrix remodeling (*C*) normalized to 18s, $n = 3$–7 mice/group. Data are presented as means ± standard error (SE). Statistical analysis was performed using two-way ANOVA with Tukey's multiple-comparisons test (*A*–*C*); $^{*}P < 0.05$, $^{**}P < 0.01$, $^{***}P < 0.001$; ns, nonsignificant. DVT, deep vein thrombosis; IL-6, interleukin-6; MCP, monocyte chemotactic protein.

thrombus at 0, 2, and 24 h after saphenous vein thrombogenesis (Fig. 6*A*). We observed that DVT initiation was similar between IL-6- and PBS-treated mice (Supplemental Videos S1 and S2), as reflected by a comparable DVT area and length at 0 h (Supplemental Fig. S6, *A* and *B*). In response to IL-6, leukocytes and platelets formed an extensive rhodamine 6 G-positive aggregate that indicates acute inflammation at the distal edge of the thrombus, mirroring the enhanced distal edge organization of IVC thrombi in the IL-6-treated mice (Fig. 6, *B* and *C*). The utilization of antibodies specific to $Ly6G^{+}Ly6C^{+}$ leukocytes confirmed a pattern similar to that of rhodamine 6 G (Supplemental Fig. S6*C*), suggesting that most of the rhodamine 6 G signals were of leukocyte origin.

Serial in vivo imaging enables the assessment of the time course of changes in DVT size (39, 69). The resulting dynamics of the thrombus area, which illustrate the resolution process, are depicted (Fig. 6*D*). Over time, both groups of mice experienced a decrease in the whole thrombus area (Fig. 6*E*). Since IL-6 facilitates the recruitment of inflammatory cells to the distal edge of DVT, we speculated that locally augmented inflammation at the edge would result in enhanced DVT resolution in that particular region. We assessed the percentage changes in the thrombus area at the ⅓ proximal and ⅓ distal edges (Fig. 6*F*). The proximal edge of the thrombus in both groups exhibited comparable thrombus area reductions at 2 and 24 h (Fig. 6, *G* and *H*). Distinctly, the distal edge of the IL-6-treated mice's thrombus demonstrated a substantially more significant reduction in thrombus area at 2 h and a higher trend at 24 h after thrombogenesis than that in

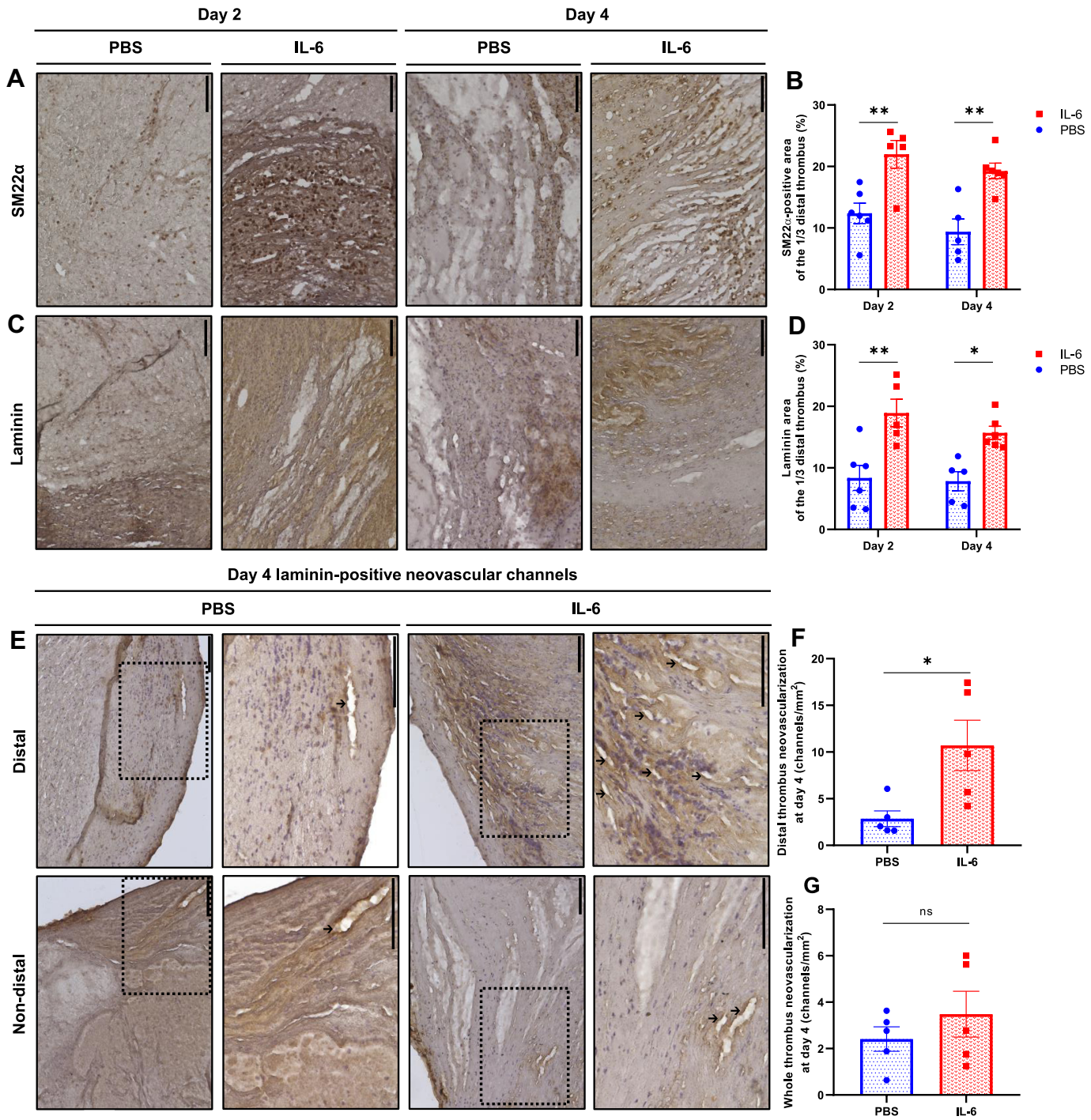

Figure 5. IL-6 promotes extracellular matrix remodeling at the distal edge of the thrombus. *A–G*: vein wall-free thrombi aged 2 and 4 days from PBS- and IL-6-treated mice were longitudinally frozen-sectioned and stained for SM22α (*A* and *B*) and laminin (*C–G*). Representative images of the ⅓ distal thrombus part [*A* and *C*; ×22.2 magnification; *E*; ×22.2 (*left*) and 44.4× (*right*) magnification; scale bar = 100 μm] with the corresponding quantifications of SM22α$^+$ myofibroblast populations, laminin area, and *day 4* laminin-positive neovascular channels (marked by black arrows) (*B*, *D*, *F*, and *G*, respectively). Data are presented as means ± standard error (SE). Statistical analysis was performed using two-way ANOVA with Tukey's multiple-comparisons test (*B* and *D*) and unpaired *t* test with Welch's correction (*F* and *G*); *$P < 0.05$, **$P < 0.01$; ns, nonsignificant; $n = 5$ or 6 mice/group. IL-6, interleukin-6; PBS, phosphate-buffered saline.

PBS-treated mice (Fig. 6, *I* and *J*), implying that IL-6 promoted DVT resolution at the distal edge. Next, we evaluated the association between the degree of inflammation and DVT resolution. As such, the extent of distal edge leukocyte-platelet accumulation unveiled a strong positive correlation with thrombus distal area reduction (Fig. 6*K*). These data reaffirm that thrombus organization, played by the acute interaction of leukocytes and platelets, to which IL-6 locally intensifies, contributes to thrombus resolution.

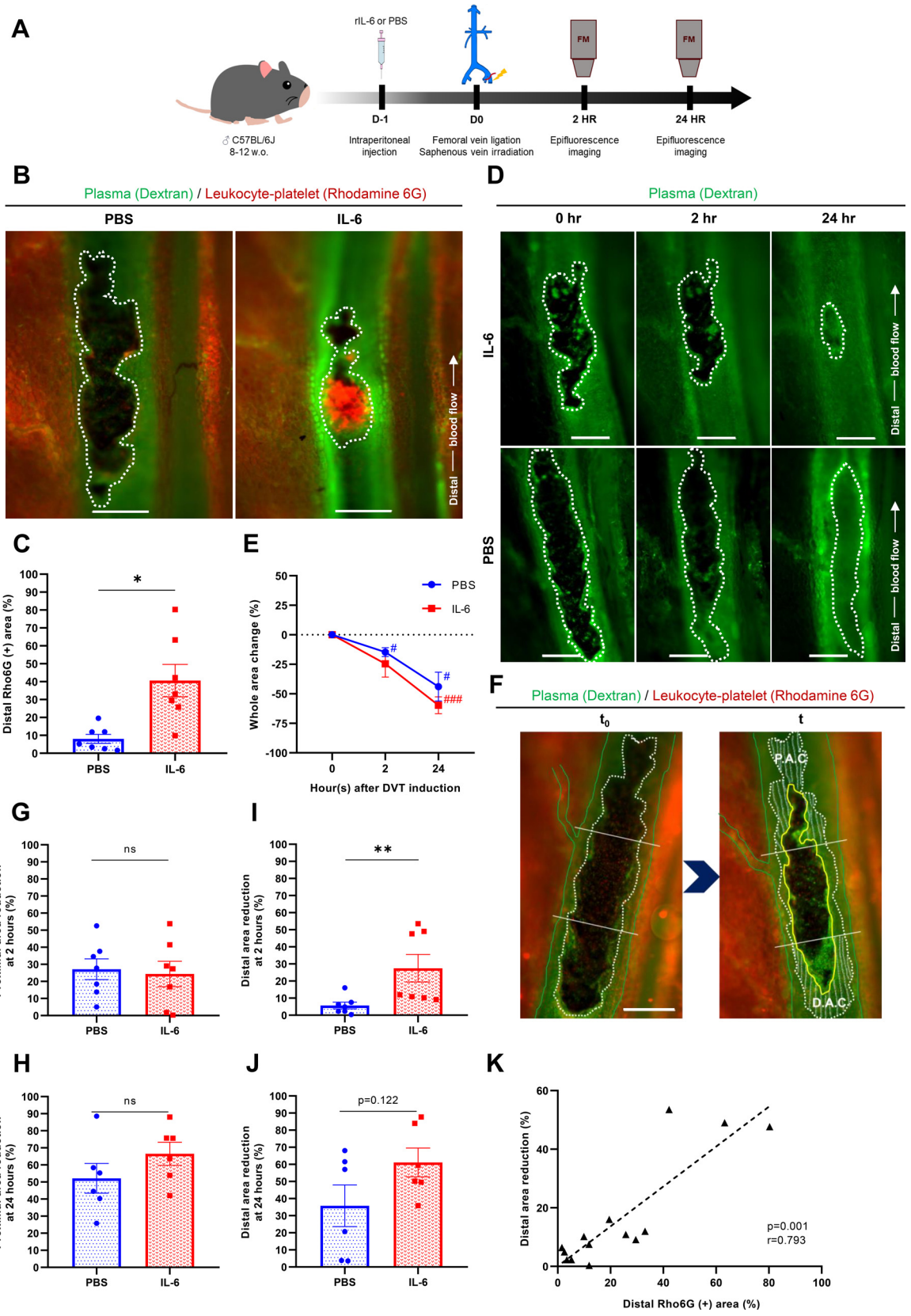

IL-6 Expedites Leukocyte Migration into the Distal Part of the Venous Thrombus

The caudal side of the DVT is reported to be the port of entry for neutrophil infiltration (69, 70). Thus, to investigate the dynamic spatiotemporal mechanism of leukocyte infiltration in the thrombus treated with IL-6 or PBS at the single-cell level, we performed serial two-photon microscopy over the saphenous vein thrombus (Fig. 7*A*). Under the influence of IL-6, leukocytes and platelets were mainly recruited to the distal edge. In contrast, we observed that the accumulation of leukocytes and platelets occurred less in number but in a more dispersed pattern in PBS-treated mice (Fig. 7*B*).

By focusing on the distal edge of the thrombus, we tracked the leukocyte migration pattern. In IL-6-treated mice, leukocytes massively migrated into the thrombus through its distal edge parallel to the venous blood flow (Fig. 7, *C* and *F*; Supplemental Video S3). In contrast, this feature was scarcely observed in the PBS group (Fig. 7, *C* and *F*; Supplemental Video S4). Quantitatively, the rhodamine 6 G-positive leukocytes of IL-6-treated mice significantly infiltrated the thrombus through the *y*-axis, in line with the direction of venous blood flow, at a longer distance than that in PBS-treated mice (Fig. 7*D*). Meanwhile, leukocytes in both groups showed similar migration distances on the *x*-axis of the thrombus (Fig. 7*E*). Furthermore, leukocytes from IL-6-treated mice exhibited amplified motility, as indicated by the faster migration speed to the saphenous vein thrombus on the *y*-axis (Fig. 7*G*), but not along the *x*-axis (Fig. 7*H*), relative to PBS-treated mice. Notably, the velocity of stasis venous blood flow was proportionate between both groups of mice (Supplemental Fig. S6*D*). This phenomenon might explain the IVC thrombus phenotype, in which IL-6 signals leukocytes to aggressively organize and resolve the thrombus from the distal edge by trailing venous flow, leading to a shorter length and lower burden.

DISCUSSION

DVT is classically believed to develop under Virchow's triad, which includes blood stasis, endothelial dysfunction, and heightened coagulability (71, 72). Recently, sterile inflammation has been a concern in DVT, with immune cells being the key players (13, 73). In the current study, we explored the role of IL-6 in the pathogenesis of acute DVT using the classical IVC stasis-induced DVT model and intravital femoral/saphenous DVT imaging model to better understand the immune cell dynamics during DVT organization and resolution.

Clinical studies have observed a significant relationship between plasma IL-6 levels and DVT. The expression of IL-6 is increased in the peripheral mononuclear cells and plasma of patients with DVT (34, 74, 75). Patients with IL-6 promoter polymorphism (−572 G > C) have also been reported to have elevated plasma IL-6 levels and an increased risk of DVT (75). A previous report has shown that persistent IL-6 overexpression in myeloid cells results in systemic inflammation and vascular dysfunction, including upregulated fibrosis and myeloid cell recruitment in arteries (28). Therefore, we speculate that IL-6 may cause venous endothelial dysfunction. In this condition, the expression of tissue factors and adhesion molecules outweighs the physiological antithrombotic properties. This contributes to the activation of coagulation cascades and the attachment of leukocytes and platelets to the endothelium, which initiates DVT formation (76, 77). Meanwhile, the effect of IL-6 on the DVT burden is conflicting in animal models. Nosaka et al. (35) reported that IL-6 supplemented in the formed thrombus of the IVC stenosis model accelerated thrombus resolution on *day 10*. Obi et al. (36) demonstrated that DVT burden increased in *IL-6*$^{-/-}$ mice on *days 8* and *21* after IVC ligation, without any alteration on *day 2*. On the contrary, Zhang et al. (34) showed that anti-IL-6 antibody treatment decreased DVT size 48 h post ligation. These conflicting shreds of evidence indicate that IL-6 has a paradoxical effect on DVT; one is a proinflammatory cytokine that augments thrombogenesis, and the other is an adaptive response to DVT organization and resolution, similar to cutaneous wound healing pathophysiology (78, 79).

Our study shows that IL-6 supplementation *1*) amplifies leukocyte infiltration, only the part of the innate but not adaptive immune system, to the distal edge of the thrombus, *2*) intensifies platelet-leukocyte activation and interactions, thereby creating acute localized inflammation that results in thrombus matrix remodeling without vein wall impairment, and *3*) leads to accelerated organization and early resolution at the distal edge. Hitherto, we established that IL-6-induced localized inflammation reduces DVT burden (Graphical Abstract).

Figure 6. Real-time epifluorescence imaging reveals IL-6-driven acute leukocyte-platelet aggregation and associated thrombus area reduction at the distal edge of the saphenous vein thrombus. *A*: schematic diagram illustrates the experimental design. Intraperitoneal (ip) injection of mouse recombinant IL-6 (rIL-6; 0.3 μg/200 μL) or PBS (200 μL) was administered to C57BL/6J mice a day before DVT induction through femoral vein ligation and laser irradiation of the saphenous vein. Serial intravital epifluorescence microscopy was performed. Images were sketched using a licensed version of Goodnotes 6.6.10. *B* and *C*: representative images of saphenous vein thrombus in PBS- and IL-6-treated mice depicting the intrathrombi aggregation of rhodamine 6 G-labeled leukocyte-platelet (*B*; scale bar = 250 μm) with the corresponding quantification of distal rhodamine 6 G-positive area (*C*). *D* and *E*: representative images of DVT resolution (*D*; scale bar = 250 μm) and quantification of the whole thrombus area change (%) in PBS- and IL-6-treated mice over 0, 2, and 24 h following DVT induction (*E*). *F*: schematic illustration of the measurement of the ⅓ proximal area change (P.A.C) and ⅓ distal area change (D.A.C) of the saphenous vein thrombus in PBS- and IL-6-treated mice; scale bar = 250 μm. The white line indicates the partition of the thrombus area relative to the lateral vessel, as an anatomical landmark. The dashed white line marks the initial thrombus area at t_0, and the yellow line demarcates the actual thrombus area at *t*: 2 or 24 h. *G* and *H*: quantitative analyses of area reduction in the ⅓ proximal part of PBS- and IL-6-treated mice saphenous vein thrombus at 2 h (*G*) and 24 h (*H*) after DVT induction. *I* and *J*: quantitative analyses of area reduction in the ⅓ distal part of the saphenous vein thrombus in PBS- and IL-6-treated mice at 2 h (*I*) and 24 h (*J*) after DVT induction. *K*: the association of the distal rhodamine 6 G-positive area with the subsequent percentage area reduction in the ⅓ distal thrombus part was assessed using Spearman's correlation. Data are presented as means ± standard error (SE). Statistical analysis was performed using the unpaired *t* test with Welch's correction (*C*, *G*, *H*, and *J*), mixed-effects model (*E*), and the Mann–Whitney test (*I*); $^{*}P < 0.05$, $^{**}P < 0.01$, vs. PBS. $\#P < 0.05$, $\#\#\#P < 0.001$ vs. 0 h; ns, nonsignificant. $n = 6$ or 7 mice/group. DVT, deep vein thrombosis; IL-6, interleukin-6; PBS, phosphate-buffered saline.

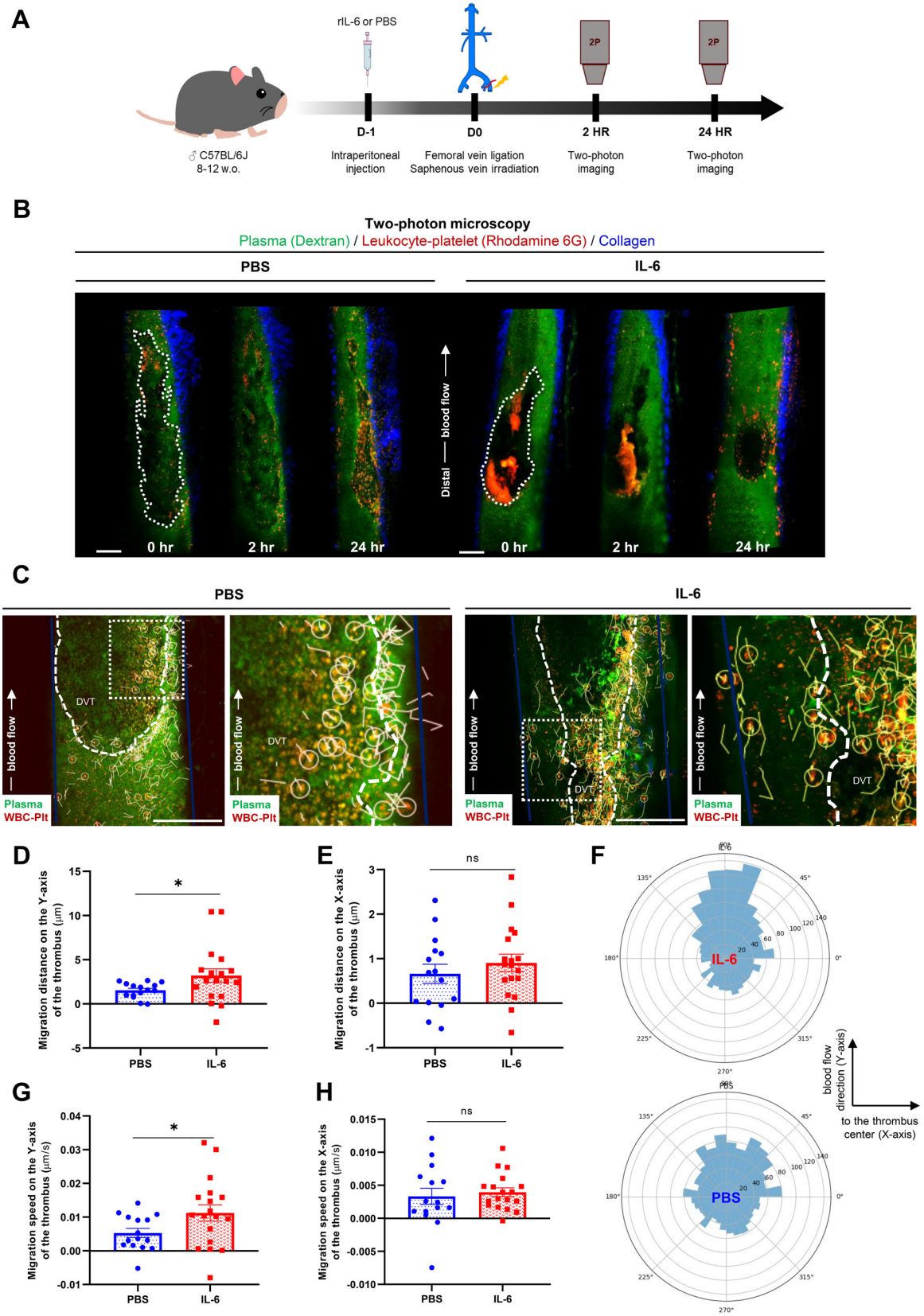

Several factors may have led to the disparities found in the studies of IL-6 in DVT. We believe that the employed thrombosis model, utilization of IL-6 genetically modified mice or antibody-based blockade, timing and route of recombinant IL-6 administration, and the phase at which the thrombus is assessed should be meticulously addressed. In terms of subacute DVT (*day 8* or later) burden, stasis, and stenosis, IVC ligation models unveiled a comparable trend in attribution with IL-6 (36). Intermittent supplementation of IL-6 in the stenosis model of subacute DVT exquisitely discovered that macrophages and various related proteolytic enzymes are the key players in reducing the DVT burden (35). However, the role of IL-6 in acute DVT (*days 2* and *4*) remains unknown. In this study, we performed pretreatment with IL-6 before DVT induction to understand the role of IL-6 in a clinical scenario in which DVT occurs in patients with severe systemic inflammation (80–84). The disadvantage of pretreatment might affect both DVT formation and resolution. However, we did not observe a significant change in thrombus formation after IL-6 treatment (Supplemental Videos S1 and S2). Correspondingly, our data revealed that IL-6 did not impair the coagulation system, even in the number of circulating blood cells at baseline. This notion is supported by the fact that the final maturation of any hematopoietic cell lineage does not require IL-6 (85), and genetic deletion of IL-6 does not dysregulate coagulation and platelet function (36) or inhibit DVT formation in mice (35, 36).

Instead of affecting thrombogenesis, IL-6 accelerated thrombus organization. Jewell et al. (86) showed that tocilizumab, an anti-IL-6R antibody, decreased the levels of coagulation factor XIII, chemerin, and plasminogen activator inhibitors. This reduction may compromise fibrin clot stability, potentially increasing the likelihood of microthrombi detachment. Identically, we showed that IL-6 supplementation promoted higher fibrin-collagen content by substituting erythrocytes within the distal part of the thrombus. Thrombus dissolution involves contraction-related size reduction and fibrotic transformation of the blood clot, in which platelets and myofibroblasts play crucial roles, leading to the restoration of luminal flow (87, 88). Collagen-rich thrombi have less porosity, implicating invulnerable fibrinolysis and firmer adherence to the venous wall (8, 36, 59, 70). Moreover, vWF found in the proximity of neutrophils and platelets reinforces the organization of DVT (10), indicating that platelets are the primary source during the acute response to IL-6 (89). Increased platelet production and reactivity induced by IL-6 have also been identified in experimental colitis, promoting microvascular thrombosis (90). In contrast, our observations demonstrate that platelets are effectors of IL-6 in DVT organization and early resolution. Through this mechanism, IL-6 can stabilize the thrombus and minimize embolization.

The effect of IL-6 on DVT, especially in the acute phase (before *day 8*), remains unclear. In the current study, using in vivo imaging techniques, we propose a novel concept that IL-6 enhances the invasion of inflammatory cells at the distal edge of DVT, resulting in locally enhanced DVT resolution. We succeeded in identifying diminished lesions by comparing the size of the same DVT over time using serial in vivo imaging of DVT, which is not possible in a classical IVC stasis-induced DVT model. Here, we demonstrated that IL-6 enhanced distal-edge dominant DVT resolution in rhodamine 6 G-positive inflamed lesions.

IL-6 is well-acknowledged to regulate cellular trafficking. Although several in vitro studies have reported the effect of IL-6 on the enhancement of cell migration capacity (91–93), no investigation has been conducted in a DVT setting. Through intravital imaging, we successfully elucidated the mode of action of IL-6 in a murine DVT model for the first time. IL-6 energizes the flow-linear infiltration of leukocytes into the distal edge of DVT, allowing aggregation with platelets. Sreeramkumar et al. (94) highlight that during migration, leukocytes exhibit asymmetrical conformation in which the leading edge (moving front) guides the movement direction and the uropod (receptor-rich trailing edge) at the back site facilitates interactions with platelets through PSGL-1 and P-selectin. In line with our previous study (69), the degree of inflammation in the initial hours of DVT could predict thrombus resolution, in which IL-6 conveys it from the distal region.

IL-6 amplified the biased migration of leukocytes in the direction of venous blood flow, independent of the velocity of stasis blood flow. We speculate that this is because the local chemokine gradient, as the effect of IL-6, is oriented on the *y*-axis of the thrombus, in which the distal edge retains the most significant concentration under the rheology of DVT formation. Global genetic deficiency of IL-6 has been shown to impair the production of local chemotactic factors (31). Our findings in this current study suggest that the in vivo assessment of leukocyte infiltration escalated by IL-6 could signify its actions in DVT resolution in real time. Such arrangements cannot be observed in the in vitro migration assays (95), where only the migration pattern is evaluated.

Figure 7. Real-time two-photon imaging demonstrates the directional leukocyte migration into DVT following IL-6 treatment. *A*: schematic diagram illustrates the experimental design. Intraperitoneal (ip) injection of mouse recombinant IL-6 (rIL-6) 0.3 μg/200 μL or PBS 200 μL was administered to C57BL/6J mice a day before DVT induction through femoral vein ligation and laser irradiation of the saphenous vein. Serial intravital two-photon microscopy was performed. Images were sketched using a licensed version of Goodnotes 6.6.10. *B*: representative images of the whole PBS- and IL-6-treated mice saphenous vein thrombus resulting from the stitching of 10–12 images by Fiji software, each captured at 0, 2, and 24 h, visualizing the pattern of acute leukocyte-platelet accumulation within the thrombus. The dashed white line indicates the initial thrombus area at 0 h. Scale bar = 100 μm. *C*–*H*: spatiotemporal dynamics of rhodamine 6 G-positive leukocyte infiltration into the distal part of PBS- and IL-6-treated mice saphenous vein thrombi were monitored using a two-photon microscope for 20–30 min. Representative images of tracked leukocyte migration (*C*; tracks of at least 76 rhodamine 6 G-positive leukocytes per mouse; scale bar = 100 μm; $n = 15$–18 mice/group) show a magnified view from the dotted white square in each group. The blue line indicates the vein wall, the dashed white line demarcates DVT, the white circle indicates infiltrating leukocytes, and the white line illustrates the tracked path of leukocytes. The quantification of the mean leukocyte migration distance on the *y*-axis, which is parallel to the direction of venous blood flow (*D*), and the *x*-axis, toward the center of the thrombus (*E*), is presented. The rose plot depicts the pattern of leukocyte infiltration into the saphenous thrombus in PBS- and IL-6-treated mice (*F*). The mean leukocyte migration speed was quantified on the *y*-axis (*G*) and *x*-axis (*H*). A negative value indicates that the leukocytes migrated in the direction opposite to the venous blood flow or outward from the thrombus center. Data were obtained for 15–18 mice/group. Data are presented as means ± standard error (SE). Statistical analysis was performed using the unpaired *t* test with Welch's correction (*D*, *E*, *G*, and *H*); $^*P < 0.05$; ns, nonsignificant. DVT, deep vein thrombosis; IL-6, interleukin-6; PBS, phosphate-buffered saline.

Limitations and Future Directions

Our study had some limitations that should be considered. IL-6 acted greater as of DVT size reduction in the total IVC ligation model than in stasis- and irradiation-induced saphenous vein thrombosis, in which partial venous blood flow surrounding the thrombus, as in the IVC stenosis model, reduced the IL-6-guided resolution (36). Since the scope of the present study was confined to targeting inflammation in the acute phase of DVT while bridging the gap of a past study where serial *days 1, 4*, and *8* of post-thrombogenesis rIL-6 treatment enhanced thrombus resolution (35), the effect of more extended continuous administration of rIL-6 in thrombus has not yet been elucidated as to whether it is deleterious and compromises DVT resolution, hence limiting the translationality of our results beyond 4 days. As mentioned earlier, persistently elevated circulating IL-6 causes maladaptive systemic inflammation and vascular dysfunction (28); thus, extensive experimental studies before clinical trials are imperative to determine the appropriate dosage and duration of IL-6 supplementation in addressing DVT. Experiments to validate the non-EndMT origins of IL-6-induced accumulation of intrathrombi myofibroblasts as part of the potential mechanisms were not feasible in the present study; thus, further multimodal exploration is advocated. Furthermore, although respecting the segmented effect of IL-6 in the generated thrombi, the thrombosed vein wall reactions to exogenous IL-6 in acute DVT development were evaluated only through histological staining due to limited tissue availability, suggesting the necessity of utilizing more advanced techniques capable of delivering quantitative assessments of small amounts of vein wall tissues.

Conclusions

In summary, we postulate that IL-6 orchestrates innate leukocytes in concert with platelets to augment acute inflammatory-dependent thrombus organization within distal specific sites, which prompts early resolution, implying the favorable contribution of IL-6 in acute DVT. Therefore, prophylactic recombinant IL-6 could potentially be sought to reduce the DVT burden in patients with inevitable occlusive thrombogenesis. Indeed, a cautious investigation into the side effects of IL-6 should be considered, although none were found in the present study. To mitigate the systemic off-target effects of IL-6, we propose that rIL-6 can be administered at the distal site of the identified venous occlusion. Transcatheter administration serves as a viable method for this purpose, although further research is required. Finally, our findings highlight the critical role of acute inflammation in thrombus organization and resolution, thereby advising caution against excessive early administration of anti-IL-6 agents in the clinical management of DVT associated with inflammatory diseases.

DATA AVAILABILITY

Data will be made available upon reasonable requests.

SUPPLEMENTAL MATERIAL

Supplemental Figs. S1–S6: https://doi.org/10.6084/m9.figshare.29432243.

Supplemental Tables S1–S3: https://doi.org/10.6084/m9.figshare.29430308.

Supplemental Videos S1–S4: https://doi.org/10.6084/m9.figshare.29430242.

GRANTS

This study was supervised and supported by the COI-NEXT program (JST Grant No. JPMJPF2018). It was also supported by Grants-in-Aid for Scientific Research from the Ministry of Education, Culture, Sports, Science, and Technology of Japan (No. 22K08117), the Lotte Foundation Research Grant, and the Kobayashi Foundation.

DISCLOSURES

No conflicts of interest, financial or otherwise, are declared by the authors.

AUTHOR CONTRIBUTIONS

A.C.A. and T.H. conceived and designed research; A.C.A. performed experiments; A.C.A., A.A., Y.S., and M.N. analyzed data; A.C.A., T.H., A.A., Y.S., M.N., K.H., H.O., and N.E. interpreted results of experiments; A.C.A. prepared figures; A.C.A. drafted manuscript; A.C.A., T.H., A.A., Y.S., M.N., K.H., H.O., and N.E. edited and revised manuscript; A.C.A., T.H., A.A., Y.S., M.N., K.H., H.O., and N.E. approved final version of manuscript.

REFERENCES

1. **Klemen ND**, **Feingold PL**, **Hashimoto B**, **Wang M**, **Kleyman S**, **Brackett A**, **Gross CP**, **Pei KY.** Mortality risk associated with venous thromboembolism: a systematic review and Bayesian meta-analysis. *Lancet Haematol* 7: e583–e593, 2020. doi:10.1016/S2352-3026(20)30211-8.
2. **Galanaud JP**, **Monreal M**, **Kahn SR.** Epidemiology of the post-thrombotic syndrome. *Thromb Res* 164: 100–109, 2018. doi:10.1016/j.thromres.2017.07.026.
3. **Lutsey PL**, **Zakai NA.** Epidemiology and prevention of venous thromboembolism. *Nat Rev Cardiol* 20: 248–262, 2023. doi:10.1038/s41569-022-00787-6.
4. **Linnemann B**, **Beyer-Westendorf J**, **Espinola-Klein C**, **Mühlberg KS**, **Müller OJ**, **Klamroth R.** Management of deep vein thrombosis: an update based on the revised AWMF S2k guideline. *Hamostaseologie* 44: 97–110, 2024. doi:10.1055/a-2178-6574.
5. **Streiff MB**, **Agnelli G**, **Connors JM**, **Crowther M**, **Eichinger S**, **Lopes R**, **McBane RD**, **Moll S**, **Ansell J.** Guidance for the treatment of deep vein thrombosis and pulmonary embolism. *J Thromb Thrombolysis* 41: 32–67, 2016 [Erratum in *J Thromb Thrombolysis* 41: 548, 2016]. doi:10.1007/s11239-016-1345-4.
6. **Freimann DG.** The structure of thrombi. In: *Hemostasis and thrombosis*, edited by Colman RW, Hirsh J, Mader VJ, Salzman EW**.** Lippincott, 1987, p. 1123–1135.
7. **Shaya SA**, **Saldanha LJ**, **Vaezzadeh N**, **Zhou J**, **Ni R**, **Gross PL.** Comparison of the effect of dabigatran and dalteparin on thrombus stability in a murine model of venous thromboembolism. *J Thromb Haemost* 14: 143–152, 2016. doi:10.1111/jth.13182.
8. **Stanford SN**, **Sabra A**, **D'Silva L**, **Lawrence M**, **Morris RH**, **Storton S**, **Brown MR**, **Evans V**, **Hawkins K**, **Williams PR**, **Davidson SJ**, **Wani M**, **Potter JF**, **Evans PA.** The changes in clot microstructure in patients with ischaemic stroke and the effects of therapeutic intervention: a prospective observational study. *BMC Neurol* 15: 35, 2015. doi:10.1186/s12883-015-0289-1.
9. **Savchenko AS**, **Martinod K**, **Seidman MA**, **Wong SL**, **Borissoff JI**, **Piazza G**, **Libby P**, **Goldhaber SZ**, **Mitchell RN**, **Wagner DD.** Neutrophil extracellular traps form predominantly during the organizing stage of human venous thromboembolism development. *J Thromb Haemost* 12: 860–870, 2014. doi:10.1111/jth.12571.
10. **Chauhan AK**, **Kisucka J**, **Lamb CB**, **Bergmeier W**, **Wagner DD.** von Willebrand factor and factor VIII are independently required to form

stable occlusive thrombi in injured veins. *Blood* 109: 2424–2429, 2007. doi:10.1182/blood-2006-06-028241.
11. **Leberzammer J**, **von Hundelshausen P.** Chemokines, molecular drivers of thromboinflammation and immunothrombosis. *Front Immunol* 14: 1276353, 2023. doi:10.3389/fimmu.2023.1276353.
12. **Henke PK**, **Wakefield T.** Thrombus resolution and vein wall injury: dependence on chemokines and leukocytes. *Thromb Res* 123, *Suppl* 2: S72–S78, 2009. doi:10.1016/S0049-3848(09)70148-3.
13. **Budnik I**, **Brill A.** Immune factors in deep vein thrombosis initiation. *Trends Immunol* 39: 610–623, 2018. doi:10.1016/j.it.2018.04.010.
14. **Nosaka M**, **Ishida Y**, **Kimura A**, **Kondo T.** Time-dependent appearance of intrathrombus neutrophils and macrophages in a stasis-induced deep vein thrombosis model and its application to thrombus age determination. *Int J Legal Med* 123: 235–240, 2009. doi:10.1007/s00414-009-0324-0.
15. **von Bruhl ML**, **Stark K**, **Steinhart A**, **Chandraratne S**, **Konrad I**, **Lorenz M**, **Khandoga A**, **Tirniceriu A**, **Coletti R**, **Köllnberger M**, **Byrne RA**, **Laitinen I**, **Walch A**, **Brill A**, **Pfeiler S**, **Manukyan D**, **Braun S**, **Lange P**, **Riegger J**, **Ware J**, **Eckart A**, **Haidari S**, **Rudelius M**, **Schulz C**, **Echtler K**, **Brinkmann V**, **Schwaiger M**, **Preissner KT**, **Wagner DD**, **Mackman N**, **Engelmann B**, **Massberg S.** Monocytes, neutrophils, and platelets cooperate to initiate and propagate venous thrombosis in mice in vivo. *J Exp Med* 209: 819–835, 2012. doi:10.1084/jem.20112322.
16. **Saha P**, **Humphries J**, **Modarai B**, **Mattock K**, **Waltham M**, **Evans CE**, **Ahmad A**, **Patel AS**, **Premaratne S**, **Lyons OT**, **Smith A.** Leukocytes and the natural history of deep vein thrombosis: current concepts and future directions. *Arterioscler Thromb Vasc Biol* 31: 506–512, 2011. doi:10.1161/ATVBAHA.110.213405.
17. **Haider P**, **Kral-Pointner JB**, **Mayer J**, **Richter M**, **Kaun C**, **Brostjan C**, **Eilenberg W**, **Fischer MB**, **Speidl WS**, **Hengstenberg C**, **Huber K**, **Wojta J**, **Hohensinner P.** Neutrophil extracellular trap degradation by differently polarized macrophage subsets. *Arterioscler Thromb Vasc Biol* 40: 2265–2278, 2020. doi:10.1161/ATVBAHA.120.314883.
18. **Humphries J**, **McGuinness CL**, **Smith A**, **Waltham M**, **Poston R**, **Burnand KG.** Monocyte chemotactic protein-1 (MCP-1) accelerates the organization and resolution of venous thrombi. *J Vasc Surg* 30: 894–899, 1999. doi:10.1016/s0741-5214(99)70014-5.
19. **Henke PK**, **Wakefield TW**, **Kadell AM**, **Linn MJ**, **Varma MR**, **Sarkar M**, **Hawley A**, **Fowlkes JB**, **Strieter RM.** Interleukin-8 administration enhances venous thrombosis resolution in a rat model. *J Surg Res* 99: 84–91, 2001. doi:10.1006/jsre.2001.6122.
20. **Varma MR**, **Varga AJ**, **Knipp BS**, **Sukheepod P**, **Upchurch GR**, **Kunkel SL**, **Wakefield TW**, **Henke PK.** Neutropenia impairs venous thrombosis resolution in the rat. *J Vasc Surg* 38: 1090–1098, 2003. doi:10.1016/s0741-5214(03)00431-2.
21. **Henke PK**, **Varga A**, **De S**, **Deatrick CB**, **Eliason J**, **Arenberg DA**, **Sukheepod P**, **Thanaporn P**, **Kunkel SL**, **Upchurch GR Jr**, **Wakefield TW.** Deep vein thrombosis resolution is modulated by monocyte CXCR2-mediated activity in a mouse model. *Arterioscler Thromb Vasc Biol* 24: 1130–1137, 2004. doi:10.1161/01.ATV.0000129537.72553.73.
22. **Henke PK**, **Pearce CG**, **Moaveni DM**, **Moore AJ**, **Lynch EM**, **Longo C**, **Varma M**, **Dewyer NA**, **Deatrick KB**, **Upchurch GR Jr**, **Wakefield TW**, **Hogaboam C**, **Kunkel SL.** Targeted deletion of CCR2 impairs deep vein thombosis resolution in a mouse model. *J Immunol* 177: 3388–3397, 2006. doi:10.4049/jimmunol.177.5.3388.
23. **Yuan H**, **Huang X**, **Ding J.** Toll-like receptor 4 deficiency in mice impairs venous thrombus resolution. *Front Mol Biosci* 10: 1165589, 2023. doi:10.3389/fmolb.2023.1165589.
24. **Hasselwander S**, **Xia N**, **Mimmler M**, **Ascher S**, **Knopp T**, **Reifenberg G**, **Karbach S**, **Ruf W**, **Reinhardt C**, **Li H.** B lymphocyte-deficiency in mice promotes venous thrombosis. *Heliyon* 8: e11740, 2022. doi:10.1016/j.heliyon.2022.e11740.
25. **Luther N**, **Shahneh F**, **Brähler M**, **Krebs F**, **Jäckel S**, **Subramaniam S**, **Stanger C**, **Schönfelder T**, **Kleis-Fischer B**, **Reinhardt C**, **Probst HC**, **Wenzel P**, **Schäfer K**, **Becker C.** Innate effector-memory T-cell activation regulates post-thrombotic vein wall inflammation and thrombus resolution. *Circ Res* 119: 1286–1295, 2016. doi:10.1161/CIRCRESAHA.116.309301.
26. **Mukhopadhyay S**, **Gabre J**, **Chabasse C**, **Bromberg JS**, **Antalis TM**, **Sarkar R.** Depletion of CD4 and CD8 positive T cells impairs venous thrombus resolution in mice. *Int J Mol Sci* 21: 1650, 2020. doi:10.3390/ijms21051650.
27. **Shahneh F**, **Grill A**, **Klein M**, **Frauhammer F**, **Bopp T**, **Schäfer K**, **Raker VK**, **Becker C.** Specialized regulatory T cells control venous blood clot resolution through SPARC. *Blood* 137: 1517–1526, 2021. doi:10.1182/blood.2020005407.
28. **Knopp T**, **Jung R**, **Wild J**, **Bochenek ML**, **Efentakis P**, **Lehmann A**, **Bieler T**, **Garlapati V**, **Richter C**, **Molitor M**, **Perius K**, **Finger S**, **Lagrange J**, **Ghasemi I**, **Zifkos K**, **Kommoss KS**, **Masri J**, **Reißig S**, **Randriamboavonjy V**, **Wunderlich T**, **Hövelmeyer N**, **Weber ANR**, **Mufazalov IA**, **Bosmann M**, **Bechmann I**, **Fleming I**, **Oelze M**, **Daiber A**, **Münzel T**, **Schäfer K**, **Wenzel P**, **Waisman A**, **Karbach S.** Myeloid cell-derived interleukin-6 induces vascular dysfunction and vascular and systemic inflammation. *Eur Heart J Open* 4: oeae046, 2024. doi:10.1093/ehjopen/oeae046.
29. **Grebenciucova E**, **VanHaerents S.** Interleukin 6: at the interface of human health and disease. *Front Immunol* 14: 1255533, 2023. doi:10.3389/fimmu.2023.1255533.
30. **Fielding CA**, **McLoughlin RM**, **McLeod L**, **Colmont CS**, **Najdovska M**, **Grail D**, **Ernst M**, **Jones SA**, **Topley N**, **Jenkins BJ.** IL-6 regulates neutrophil trafficking during acute inflammation via STAT3. *J Immunol* 181: 2189–2195, 2008. doi:10.4049/jimmunol.181.3.2189.
31. **Romano M**, **Sironi M**, **Toniatti C**, **Polentarutti N**, **Fruscella P**, **Ghezzi P**, **Faggioni R**, **Luini W**, **van Hinsbergh V**, **Sozzani S**, **Bussolino F**, **Poli V**, **Ciliberto G**, **Mantovani A.** Role of IL-6 and its soluble receptor in induction of chemokines and leukocyte recruitment. *Immunity* 6: 315–325, 1997. doi:10.1016/s1074-7613(00)80334-9.
32. **Choy EHS**, **Calabrese LH.** Neuroendocrine and neurophysiological effects of interleukin 6 in rheumatoid arthritis. *Rheumatology (Oxford)* 57: 1885–1895, 2018. doi:10.1093/rheumatology/kex391.
33. **Gabay C.** Interleukin-6 and chronic inflammation. *Arthritis Res Ther* 8, *Suppl* 4: S3, 2006. doi:10.1186/ar1917.
34. **Zhang Y**, **Zhang Z**, **Wei R**, **Miao X**, **Sun S**, **Liang G**, **Chu C**, **Zhao L**, **Zhu X**, **Guo Q**, **Wang B**, **Li X.** IL (Interleukin)-6 contributes to deep vein thrombosis and is negatively regulated by miR-338-5p. *Arterioscler Thromb Vasc Biol* 40: 323–334, 2020. doi:10.1161/ATVBAHA.119.313137.
35. **Nosaka M**, **Ishida Y**, **Kimura A**, **Kuninaka Y**, **Taruya A**, **Ozaki M**, **Tanaka A**, **Mukaida N**, **Kondo T.** Crucial involvement of IL-6 in thrombus resolution in mice via macrophage recruitment and the induction of proteolytic enzymes. *Front Immunol* 10: 3150, 2019. doi:10.3389/fimmu.2019.03150.
36. **Obi AT**, **Sharma SB**, **Elfline MA**, **Luke CE**, **Dowling AR**, **Cai Q**, **Kimball AS**, **Hollinstat M**, **Stanger L**, **Moore BB**, **Jaffer FA**, **Henke PK.** Experimental venous thrombus resolution is driven by IL-6 mediated monocyte actions. *Sci Rep* 13: 3253, 2023. doi:10.1038/s41598-023-30149-2.
37. **Dowling AR**, **Luke CE**, **Cai Q**, **Pellerito AM**, **Obi AT**, **Henke PK.** Modulation of interleukin-6 and its effect on late vein wall injury in a stasis mouse model of deep vein thrombosis. *JVS Vasc Sci* 3: 246–255, 2022. doi:10.1016/j.jvssci.2022.04.001.
38. **Hara T**, **Ughi GJ**, **McCarthy JR**, **Erdem SS**, **Mauskapf A**, **Lyon SC**, **Fard AM**, **Edelman ER**, **Tearney GJ**, **Jaffer FA.** Intravascular fibrin molecular imaging improves the detection of unhealed stents assessed by optical coherence tomography in vivo. *Eur Heart J* 38: 447–455, 2017. doi:10.1093/eurheartj/ehv677.
39. **Ripplinger CM**, **Kessinger CW**, **Li C**, **Kim JW**, **McCarthy JR**, **Weissleder R**, **Henke PK**, **Lin CP**, **Jaffer FA.** Inflammation modulates murine venous thrombosis resolution in vivo: assessment by multimodal fluorescence molecular imaging. *Arterioscler Thromb Vasc Biol* 32: 2616–2624, 2012. doi:10.1161/ATVBAHA.112.251983.
40. **Hara T**, **Truelove J**, **Tawakol A**, **Wojtkiewicz GR**, **Hucker WJ**, **MacNabb MH**, **Brownell AL**, **Jokivarsi K**, **Kessinger CW**, **Jaff MR**, **Henke PK**, **Weissleder R**, **Jaffer FA.** 18F-fluorodeoxyglucose positron emission tomography/computed tomography enables the detection of recurrent same-site deep vein thrombosis by illuminating recently formed, neutrophil-rich thrombus. *Circulation* 130: 1044–1052, 2014. doi:10.1161/CIRCULATIONAHA.114.008902.
41. **Okano M**, **Hara T**, **Nishimori M**, **Irino Y**, **Satomi-Kobayashi S**, **Shinohara M**, **Toh R**, **Jaffer FA**, **Ishida T**, **Hirata KI.** In vivo imaging of venous thrombus and pulmonary embolism using novel murine venous thromboembolism model. *JACC Basic Transl Sci* 5: 344–356, 2020. doi:10.1016/j.jacbts.2020.01.010.
42. **Lind MM**, **Johansson M**, **Själander A**, **Johansson L.** Incidence and risk factors of venous thromboembolism in men and women. *Thromb Res* 214: 82–86, 2022. doi:10.1016/j.thromres.2022.04.014.

43. **Roach RE**, **Cannegieter SC**, **Lijfering WM.** Differential risks in men and women for first and recurrent venous thrombosis: the role of genes and environment. *J Thromb Haemost* 12: 1593–1600, 2014. doi:10.1111/jth.12678.
44. **Wong JH**, **Dukes J**, **Levy RE**, **Sos B**, **Mason SE**, **Fong TS**, **Weiss EJ.** Sex differences in thrombosis in mice are mediated by sex-specific growth hormone secretion patterns. *J Clin Invest* 118: 2969–2978, 2008. doi:10.1172/JCI34957.
45. **Diaz JA**, **Saha P**, **Cooley B**, **Palmer OR**, **Grover SP**, **Mackman N**, **Wakefield TW**, **Henke PK**, **Smith A**, **Lal BK.** Choosing a mouse model of venous thrombosis. *Arterioscler Thromb Vasc Biol* 39: 311–318, 2019. doi:10.1161/ATVBAHA.118.311818.
46. **Alvarado CM**, **Diaz JA**, **Hawley AE**, **Wrobleski SK**, **Sigler RE**, **Myers DD Jr.** Male mice have increased thrombotic potential: sex differences in a mouse model of venous thrombosis. *Thromb Res* 127: 478–486, 2011. doi:10.1016/j.thromres.2011.01.004.
47. **Chernysh IN**, **Mukhopadhyay S**, **Johnson TA**, **Brooks JA**, **Sarkar R**, **Weisel JW**, **Antalis TM.** Time-dependent ultrastructural changes during venous thrombogenesis and thrombus resolution. *J Thromb Haemost* 22: 1675–1688, 2024. doi:10.1016/j.jtha.2024.02.020.
48. **Rys RN**, **Blostein MD**, **Lemarié CA.** Deep vein thrombosis induced by stasis in mice monitored by high frequency ultrasonography. *J Vis Exp* 13: 57392, 2018. doi:10.3791/57392.
49. **Diaz JA**, **Obi AT**, **Myers DD Jr**, **Wrobleski SK**, **Henke PK**, **Mackman N**, **Wakefield TW.** Critical review of mouse models of venous thrombosis. *Arterioscler Thromb Vasc Biol* 32: 556–562, 2012. doi:10.1161/ATVBAHA.111.244608.
50. **Schönfelder T**, **Jäckel S**, **Wenzel P.** Mouse models of deep vein thrombosis. *Gefasschirurgie* 22: 28–33, 2017. doi:10.1007/s00772-016-0227-6.
51. **Brandt M**, **Schönfelder T**, **Schwenk M**, **Becker C**, **Jäckel S**, **Reinhardt C**, **Stark K**, **Massberg S**, **Münzel T**, **von Brühl ML**, **Wenzel P.** Deep vein thrombus formation induced by flow reduction in mice is determined by venous side branches. *Clin Hemorheol Microcirc* 56: 145–152, 2014. doi:10.3233/CH-131680.
52. **Kiouptsi K**, **Casari M**, **Mandel J**, **Gao Z**, **Deppermann C.** Intravital imaging of thrombosis models in mice. *Hamostaseologie* 43: 348–359, 2023. doi:10.1055/a-2118-2932.
53. **Livak KJ**, **Schmittgen TD.** Analysis of relative gene expression data using real-time quantitative PCR and the 2(-Delta Delta C(T)) method. *Methods* 25: 402–408, 2001. doi:10.1006/meth.2001.1262.
54. **Raykin J**, **Snider E**, **Bheri S**, **Mulvihill J**, **Ethier CR.** A modified gelatin zymography technique incorporating total protein normalization. *Anal Biochem* 521: 8–10, 2017. doi:10.1016/j.ab.2017.01.003.
55. **Deguchi JO**, **Aikawa M**, **Tung CH**, **Aikawa E**, **Kim DE**, **Ntziachristos V**, **Weissleder R**, **Libby P.** Inflammation in atherosclerosis: visualizing matrix metalloproteinase action in macrophages in vivo. *Circulation* 114: 55–62, 2006. doi:10.1161/CIRCULATIONAHA.106.619056.
56. **Ershov D**, **Phan MS**, **Pylvänäinen JW**, **Rigaud SU**, **Le Blanc L**, **Charles-Orszag A**, **Conway JRW**, **Laine RF**, **Roy NH**, **Bonazzi D**, **Duménil G**, **Jacquemet G**, **Tinevez JY.** TrackMate 7: integrating state-of-the-art segmentation algorithms into tracking pipelines. *Nat Methods* 19: 829–832, 2022. doi:10.1038/s41592-022-01507-1.
57. **Tinevez JY**, **Perry N**, **Schindelin J**, **Hoopes GM**, **Reynolds GD**, **Laplantine E**, **Bednarek SY**, **Shorte SL**, **Eliceiri KW.** TrackMate: an open and extensible platform for single-particle tracking. *Methods* 115: 80–90, 2017. doi:10.1016/j.ymeth.2016.09.016.
58. **Kung SH**, **Hagstrom JN**, **Cass D**, **Tai SJ**, **Lin HF**, **Stafford DW**, **High KA.** Human factor IX corrects the bleeding diathesis of mice with hemophilia B. *Blood* 91: 784–790, 1998.
59. **Czaplicki C**, **Albadawi H**, **Partovi S**, **Gandhi RT**, **Quencer K**, **Deipolyi AR**, **Oklu R.** Can thrombus age guide thrombolytic therapy? *Cardiovasc Diagn Ther* 7: S186–S196, 2017. doi:10.21037/cdt.2017.11.05.
60. **Grover SP**, **Evans CE**, **Patel AS**, **Modarai B**, **Saha P**, **Smith A.** Assessment of venous thrombosis in animal models. *Arterioscler Thromb Vasc Biol* 36: 245–252, 2016. doi:10.1161/ATVBAHA.115.306255.
61. **Henke PK**, **Nicklas JM**, **Obi A.** Immune cell-mediated venous thrombus resolution. *Res Pract Thromb Haemost* 7: 102268, 2023. doi:10.1016/j.rpth.2023.102268.
62. **Wakefield TW**, **Myers DD**, **Henke PK.** Mechanisms of venous thrombosis and resolution. *Arterioscler Thromb Vasc Biol* 28: 387–391, 2008. doi:10.1161/ATVBAHA.108.162289.
63. **Ludwig N**, **Hilger A**, **Zarbock A**, **Rossaint J.** Platelets at the crossroads of pro-inflammatory and resolution pathways during inflammation. *Cells* 11: 1957, 2022. doi:10.3390/cells11121957.
64. **Mukhopadhyay S**, **Johnson TA**, **Duru N**, **Buzza MS**, **Pawar NR**, **Sarkar R**, **Antalis TM.** Fibrinolysis and inflammation in venous thrombus resolution. *Front Immunol* 10: 1348, 2019. doi:10.3389/fimmu.2019.01348.
65. **Hinz B.** The role of myofibroblasts in wound healing. *Curr Res Transl Med* 64: 171–177, 2016. doi:10.1016/j.retram.2016.09.003.
66. **Lee YU**, **Lee AY**, **Humphrey JD**, **Rausch MK.** Histological and biomechanical changes in a mouse model of venous thrombus remodeling. *Biorheology* 52: 235–245, 2015. doi:10.3233/BIR-15058.
67. **Halper J.** Basic components of connective tissues and extracellular matrix: fibronectin, fibrinogen, laminin, elastin, fibrillins, fibulins, matrilins, tenascins and thrombospondins. *Adv Exp Med Biol* 1348: 105–126, 2021. doi:10.1007/978-3-030-80614-9_4.
68. **Loinard C**, **Benadjaoud MA**, **Lhomme B**, **Flamant S**, **Baijer J**, **Tamarat R.** Inflammatory cells dynamics control neovascularization and tissue healing after localized radiation induced injury in mice. *Commun Biol* 6: 571, 2023. doi:10.1038/s42003-023-04939-3.
69. **Adinata A**, **Hara T**, **Achyar AC**, **Suzuki Y**, **Hirata KI**, **Otake H**, **Emoto N.** Usefulness of serial in vivo imaging to directly assess the role of inflammation in thrombus resolution and organization. *Biochem Biophys Res Commun* 747: 151293, 2025. doi:10.1016/j.bbrc.2025.151293.
70. **Kral-Pointner JB**, **Haider P**, **Szabo PL**, **Salzmann M**, **Brekalo M**, **Schneider KH**, **Schrottmaier WC**, **Kaun C**, **Bleichert S**, **Kiss A**, **Sickha R**, **Hengstenberg C**, **Huber K**, **Brostjan C**, **Bergmeister H**, **Assinger A**, **Podesser BK**, **Wojta J**, **Hohensinner P.** Reduced monocyte and neutrophil infiltration and activation by P-selectin/CD62P inhibition enhances thrombus resolution in mice. *Arterioscler Thromb Vasc Biol* 44: 954–968, 2024. doi:10.1161/ATVBAHA.123.320016.
71. **Reitsma PH**, **Versteeg HH**, **Middeldorp S.** Mechanistic view of risk factors for venous thromboembolism. *Arterioscler Thromb Vasc Biol* 32: 563–568, 2012. doi:10.1161/ATVBAHA.111.242818.
72. **Stone J**, **Hangge P**, **Albadawi H**, **Wallace A**, **Shamoun F**, **Knuttien MG**, **Naidu S**, **Oklu R.** Deep vein thrombosis: pathogenesis, diagnosis, and medical management. *Cardiovasc Diagn Ther* 7: S276–S284, 2017. doi:10.21037/cdt.2017.09.01.
73. **Nicklas JM**, **Gordon AE**, **Henke PK.** Resolution of deep venous thrombosis: proposed immune paradigms. *Int J Mol Sci* 21: 2080, 2020. doi:10.3390/ijms21062080.
74. **Salemi R**, **Gattuso G**, **Tomasello B**, **Lavoro A**, **Gaudio A**, **Libra M**, **Signorelli SS**, **Candido S.** Co-occurrence of interleukin-6 receptor Asp358Ala variant and high plasma levels of IL-6: an evidence of IL-6 trans-signaling activation in deep vein thrombosis (DVT) patients. *Biomolecules* 12: 681, 2022. doi:10.3390/biom12050681.
75. **Sharma A**, **Singh K**, **Biswas A**, **Ranjan R**, **Kishor K**, **Pandey H**, **Kumar R**, **Mahapatra M**, **Oldenburg J**, **Saxena R.** Impact of interleukin 6 promoter polymorphisms (-174 G > C, -572 G > C and -597 G > A) on plasma IL-6 levels and their influence on the development of DVT: a study from India. *Hematology* 23: 833–838, 2018. doi:10.1080/10245332.2018.1483546.
76. **Donadini MP**, **Calcaterra F**, **Romualdi E**, **Ciceri R**, **Cancellara A**, **Lodigiani C**, **Bacci M**, **Della Bella S**, **Ageno W**, **Mavilio D.** The link between venous and arterial thrombosis: is there a role for endothelial dysfunction? *Cells* 14: 144, 2025. doi:10.3390/cells14020144.
77. **Colling ME**, **Tourdot BE**, **Kanthi Y.** Inflammation, infection and venous thromboembolism. *Circ Res* 128: 2017–2036, 2021. doi:10.1161/CIRCRESAHA.121.318225.
78. **Lin ZQ**, **Kondo T**, **Ishida Y**, **Takayasu T**, **Mukaida N.** Essential involvement of IL-6 in the skin wound-healing process as evidenced by delayed wound healing in IL-6-deficient mice. *J Leukoc Biol* 73: 713–721, 2003. doi:10.1189/jlb.0802397.
79. **McFarland-Mancini MM**, **Funk HM**, **Paluch AM**, **Zhou M**, **Giridhar PV**, **Mercer CA**, **Kozma SC**, **Drew AF.** Differences in wound healing in mice with deficiency of IL-6 versus IL-6 receptor. *J Immunol* 184: 7219–7228, 2010. doi:10.4049/jimmunol.0901929.
80. **Hozumi H**, **Russell J**, **Vital S**, **Granger DN.** IL-6 mediates the intestinal microvascular thrombosis associated with experimental colitis. *Inflamm Bowel Dis* 22: 560–568, 2016. doi:10.1097/MIB.0000000000000656.
81. **Cerletti C**, **de Gaetano G**, **Lorenzet R.** Platelet - leukocyte interactions: multiple links between inflammation, blood coagulation and

vascular risk. *Mediterr J Hematol Infect Dis* 2: e2010023, 2010. doi:10.4084/MJHID.2010.023.

82. **Liu H**, **Guo N**, **Zheng Q**, **Zhang Q**, **Chen J**, **Cai Y**, **Luo Q**, **Xu Q**, **Chen X**, **Yang S**, **Zhang S.** Association of interleukin-6, ferritin, and lactate dehydrogenase with venous thromboembolism in COVID-19: a systematic review and meta-analysis. *BMC Infect Dis* 24: 324, 2024. doi:10.1186/s12879-024-09205-3.
83. **Rabinovich A**, **Cohen JM**, **Cushman M**, **Kahn SR**, **Bio SOXI**; **BioSOX Investigators.** Association between inflammation biomarkers, anatomic extent of deep venous thrombosis, and venous symptoms after deep venous thrombosis. *J Vasc Surg Venous Lymphat Disord* 3: 347–353.e1, 2015. doi:10.1016/j.jvsv.2015.04.005.
84. **Saghazadeh A**, **Rezaei N.** Inflammation as a cause of venous thromboembolism. *Crit Rev Oncol Hematol* 99: 272–285, 2016. doi:10.1016/j.critrevonc.2016.01.007.
85. **Maeda K**, **Baba Y**, **Nagai Y**, **Miyazaki K**, **Malykhin A**, **Nakamura K**, **Kincade PW**, **Sakaguchi N**, **Coggeshall KM.** IL-6 blocks a discrete early step in lymphopoiesis. *Blood* 106: 879–885, 2005. doi:10.1182/blood-2005-02-0456.
86. **Jewell P**, **Ansorge O**, **Kuker W**, **Irani SR**, **Zamboni G.** Tocilizumab-associated multifocal cerebral thrombotic microangiopathy. *Neurol Clin Pract* 6: e24–e26, 2016. doi:10.1212/CPJ.0000000000000220.
87. **Litvinov RI**, **Weisel JW.** Blood clot contraction: mechanisms, pathophysiology, and disease. *Res Pract Thromb Haemost* 7: 100023, 2023. doi:10.1016/j.rpth.2022.100023.
88. **Che Y**, **Chien Y**, **Zhu Y**, **Huang X**, **Wu L**, **Ai Y**, **Jiang S**, **Li F**, **Chen S.** GSDMD-dependent neutrophil extracellular traps mediate portal vein thrombosis and associated fibrosis in cirrhosis. *Int J Mol Sci* 25: 9099, 2024. doi:10.3390/ijms25169099.
89. **Bryckaert M**, **Rosa JP**, **Denis CV**, **Lenting PJ.** Of von Willebrand factor and platelets. *Cell Mol Life Sci* 72: 307–326, 2015. doi:10.1007/s00018-014-1743-8.
90. **Senchenkova EY**, **Komoto S**, **Russell J**, **Almeida-Paula LD**, **Yan LS**, **Zhang S**, **Granger DN.** Interleukin-6 mediates the platelet abnormalities and thrombogenesis associated with experimental colitis. *Am J Pathol* 183: 173–181, 2013. doi:10.1016/j.ajpath.2013.03.014.
91. **Chuang JY**, **Huang YL**, **Yen WL**, **Chiang IP**, **Tsai MH**, **Tang CH.** Syk/JNK/AP-1 signaling pathway mediates interleukin-6-promoted cell migration in oral squamous cell carcinoma. *Int J Mol Sci* 15: 545–559, 2014. doi:10.3390/ijms15010545.
92. **Razidlo GL**, **Burton KM**, **McNiven MA.** Interleukin-6 promotes pancreatic cancer cell migration by rapidly activating the small GTPase CDC42. *J Biol Chem* 293: 11143–11153, 2018. doi:10.1074/jbc.RA118.003276.
93. **Valenca-Pereira F**, **Fang Q**, **Marié IJ**, **Giddings EL**, **Fortner KA**, **Yang R**, **Villarino AV**, **Huang YH**, **Frank DA**, **Wen H**, **Levy DE**, **Rincon M.** IL-6 enhances CD4 cell motility by sustaining mitochondrial Ca^{2+} through the noncanonical STAT3 pathway. *Proc Natl Acad Sci USA* 118: e2103444118, 2021. doi:10.1073/pnas.2103444118.
94. **Sreeramkumar V**, **Adrover JM**, **Ballesteros I**, **Cuartero MI**, **Rossaint J**, **Bilbao I**, **Nácher M**, **Pitaval C**, **Radovanovic I**, **Fukui Y**, **McEver RP**, **Filippi MD**, **Lizasoain I**, **Ruiz-Cabello J**, **Zarbock A**, **Moro MA**, **Hidalgo A.** Neutrophils scan for activated platelets to initiate inflammation. *Science* 346: 1234–1238, 2014. doi:10.1126/science.1256478.
95. **Frattolin J**, **Watson DJ**, **Bonneuil WV**, **Russell MJ**, **Fasanella Masci F**, **Bandara M**, **Brook BS**, **Nibbs RJB**, **Moore JE Jr.** The critical importance of spatial and temporal scales in designing and interpreting immune cell migration assays. *Cells* 10: 3439, 2021. doi:10.3390/cells10123439.